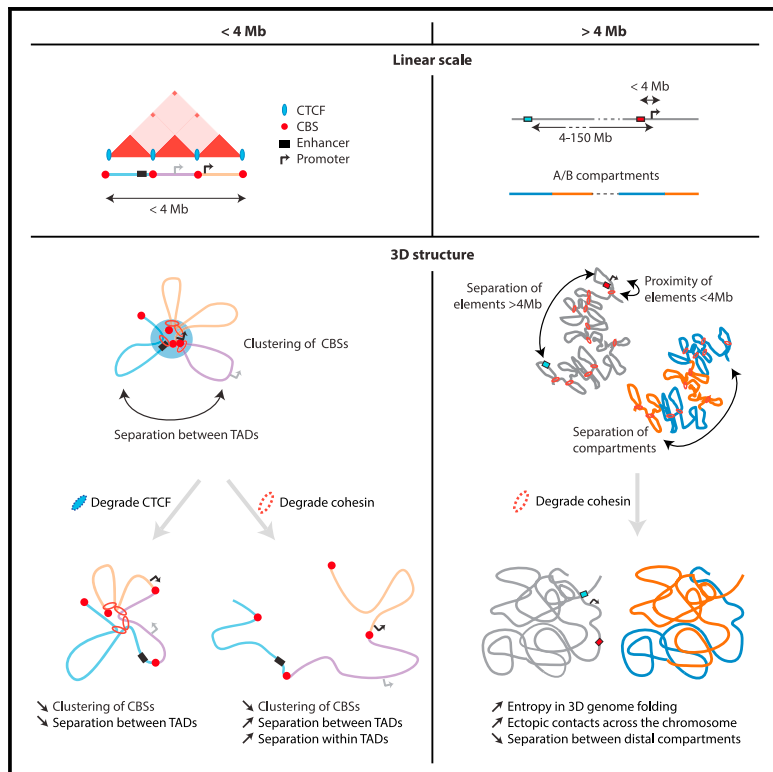


Loop stacking organizes genome folding from TADs to chromosomes

Graphical abstract



Authors

Antonina Hafner, Minhee Park,
Scott E. Berger, Sedona E. Murphy,
Elphège P. Nora, Alistair N. Boettiger

Correspondence

boettiger@stanford.edu

In brief

Hafner et al. use microscopy to trace folding of individual chromosomes. They observe and quantify chromatin loops and find that loop stacking is important for 3D organization across genomic scales. CTCF is important for preferential clustering of TAD-boundary sites. Cohesin is essential for both TAD and chromosome-scale folding.

Highlights

- Chromosome tracing shows radially organized chromosome loops
- CTCF boundary sites form hubs that depend on cohesin and CTCF
- Loss of cohesin leads to expansion at the <4 Mb scale and increased mixing at >4 Mb scale
- Loss of cohesin increases entropy in genome folding and variation in gene expression



Article

Loop stacking organizes genome folding from TADs to chromosomes

Antonina Hafner,¹ Minhee Park,^{1,6} Scott E. Berger,² Sedona E. Murphy,^{1,3} Elphège P. Nora,^{4,5} and Alistair N. Boettiger^{1,7,*}

¹Department of Developmental Biology, Stanford University, Stanford, CA, USA

²Biophysics Program, Stanford University, Stanford, CA, USA

³Department of Genetics, Stanford University, Stanford, CA, USA

⁴Cardiovascular Research Institute, University of California, San Francisco, San Francisco, CA, USA

⁵Department of Biochemistry and Biophysics, University of California, San Francisco, San Francisco, CA, USA

⁶Present address: Department of Biological Sciences, Korea Advanced Institute of Science and Technology, Daejeon, Republic of Korea

⁷Lead contact

*Correspondence: boettiger@stanford.edu

<https://doi.org/10.1016/j.molcel.2023.04.008>

SUMMARY

Although population-level analyses revealed significant roles for CTCF and cohesin in mammalian genome organization, their contributions at the single-cell level remain incompletely understood. Here, we used a super-resolution microscopy approach to measure the effects of removal of CTCF or cohesin in mouse embryonic stem cells. Single-chromosome traces revealed cohesin-dependent loops, frequently stacked at their loop anchors forming multi-way contacts (hubs), bridging across TAD boundaries. Despite these bridging interactions, chromatin in intervening TADs was not intermixed, remaining separated in distinct loops around the hub. At the multi-TAD scale, steric effects from loop stacking insulated local chromatin from ultra-long range (>4 Mb) contacts. Upon cohesin removal, the chromosomes were more disordered and increased cell-cell variability in gene expression. Our data revise the TAD-centric understanding of CTCF and cohesin and provide a multi-scale, structural picture of how they organize the genome on the single-cell level through distinct contributions to loop stacking.

INTRODUCTION

Cohesin and CTCF are essential for the establishment and maintenance of proper genome folding and have been most recognized for folding the genome into topologically associating domains (TADs). Indeed, cohesin and CTCF binding is enriched at TAD boundaries, and acute depletion of these proteins has been shown by Hi-C and imaging to lead to loss of TADs.^{1–5} Polymer modeling work has proposed that these two proteins work together in forming TADs through distinct roles; cohesin extrudes loops of chromatin but stalls at sites bound by CTCF,^{6,7} and considerable evidence supports these molecular roles.⁸ However, a detailed view of the 3D structures of single chromosomes and how they are perturbed on the removal of cohesin or CTCF, with resolution from TADs to whole chromosomes, is lacking. Such a high-resolution view may tease apart regimes in which cohesin and CTCF operate that are not distinguished by pairwise ensemble averages and thus help us better understand how they affect the *cis*-regulation of transcription. Microscopy approaches are well suited for investigating the 3D structure and heterogeneity at the single-cell level.

Recent imaging approaches to study the effects of cohesin and CTCF on the chromosome organization in single cells

have not provided a complete or fully concordant picture. Our earlier work found that single cells exhibited “TAD-like” domains, which were preserved in the absence of cohesin, although the position of their borders became more randomly distributed, leading to the loss of true (population level) TADs.³ Two more recent microscopy studies that labeled TADs with and without cohesin also observed globular chromatin volumes in both conditions but reported conflicting observations on the effect of cohesin loss.^{9,10} On degrading cohesin, Luppino and colleagues found a reduced overlap between adjacently labeled TADs, whereas the volume of the TADs remained the same. By contrast, the second imaging study by Szabo and colleagues found that the loss of cohesin did not significantly change the overlap between adjacently labeled TADs but increased the volume of each TAD. To our knowledge to date, there are also no studies investigating how the changes at the TAD scale affect single-chromosome folding at larger genomic scales. There is also limited data on how these factors affect multi-way contacts in a sequence-dependent manner.^{3,11}

To better understand the role of cohesin and CTCF on the genome structure, using a multi-scale chromosome tracing approach, similar to recent reports,^{12–14} we imaged chromatin



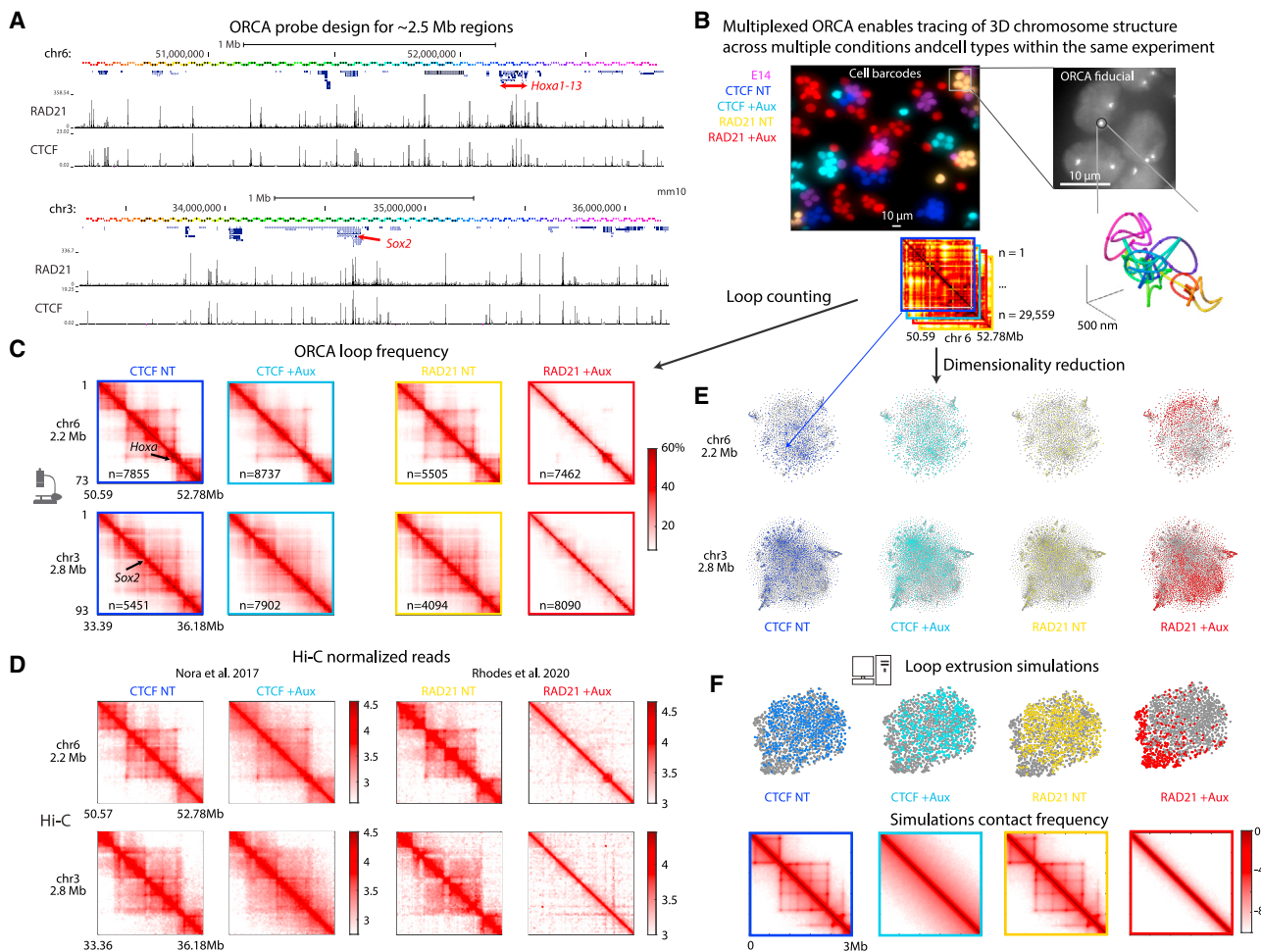


Figure 1. A multiplexed approach for chromosome tracing

(A) UCSC genome tracks showing the tiling of ORCA readout probes (Tables S1 and S2) for the chr6 and chr3 ~2.5 Mb-sized regions.

(B) Example of a field of view with pseudo-colored cell barcode labels for all imaged conditions: mES parental E14 cell line, CTCF-AID, and RAD21-AID auxin-treated (+Aux) or untreated (NT) cells. Fiducial signal (labeling all readout probes in the domain) is shown as well as an example trace of a single chromosome (blow-out). Single chromosome traces can be plotted as 3D traces (tube radius is 15 nm, sphere radius is 20 nm) or as single-chromosome pairwise distance maps. Colored borders on maps denote cell barcodes. These distance maps are used to calculate loop frequency (C) and reduced to two-dimensional t-SNE plots (E), where each map is represented by a single dot in t-SNE space and where dot color denotes cell barcodes.

(C) ORCA loop frequency maps, computed from the single trace maps described in (B).

(D) Hi-C data for the same chr6 and chr3 domains imaged by ORCA.

(E) t-SNE analysis on ORCA single-chromosome maps.

(F) t-SNE plots and contact frequency maps from simulated polymers for a 3 Mb-sized domain.

in mouse embryonic stem cells (mESCs), from the scale of loop-dots and TADs to the scale of chromosomes and compartments. To accelerate this investigation, we developed a method to multiplex this imaging and so combine different genetically edited cell lines and different treatment conditions into a single experiment, enabling direct measurement of the 3D structure in nanometers without the risk of batch effects. Our single-chromosome data provide a detailed view of how cohesin and CTCF shape the 3D structure of the chromatin; enhancing the local contact by forming heterogeneous loops at sub-megabase scales, preventing the distal contact by loop clash at megabase scales and facilitating TAD-border bypass by forming hubs of loop anchors.

RESULTS

Rapid optical profiling of chromatin structure

We used auxin inducible protein degradation (AID) to acutely deplete either CTCF or cohesin^{1,10} (Figure S1A) and used optical reconstruction of chromatin architecture (ORCA)¹⁵ to measure the effects on chromatin folding. We initially focused on two regions on chromosomes 6 and 3, each ~2.5 Mb, which in mESCs exhibit multiple TADs, sub-TADs, and loop-dots, along with highly studied genes (the *Hoxa* cluster and the *Sox2* gene) (Figure 1A). These regions were divided into 73 or 93 30-kb target-segments for ORCA labeling (Tables S1 and S2), balancing throughput, and genomic coverage in the assay and on par

with the effective resolution of recent Hi-C data from these cells for resolving sub-TADs and loop-dots^{1,4} (Figure S1B).

To enable fast imaging of multiple treatment conditions and to control for potential batch effects intrinsic to high-content, high-resolution assays, we developed a multiplexed ORCA approach (Figure 1B). We adapted a recently published method from single-cell sequencing¹⁶ to attach distinct oligonucleotide-barcodes to the cell surface, after which cells can be combined, hybridized with ORCA probes, and imaged within the same experiment, where cell surface barcodes are read out by sequential hybridization, similar to ORCA barcodes (Figure 1B). This reduced imaging time from 5 weeks to 1 week to cover 5 conditions: CTCF-AID and RAD21-AID endogenously tagged cells, either not treated (NT) or treated with auxin for 4 h (+Aux) to degrade CTCF or the RAD21 sub-unit of cohesin (Figure S1A), and the parental E14 mESC line from which these were made. We quantified for each condition the frequency that any step of the traced sequence came in contact (i.e., looped) with any other step along the trace. We used the average distance between adjacent steps as the cutoff distance for calling a contact/loop, since adjacent steps are tiled without gaps (Figure 1A). This selection takes advantage of the internal control provided by adjacent probes and avoids the need to choose an arbitrary cutoff distance. We plotted the resulting pairwise contact frequencies (loop frequencies) as a heatmap (Figure 1C). Note the units in these maps are the percentage (0%–100%) of traces in the population exhibiting the given loop, not a normalized or matrix-balanced read count. Replicate experiments showed high reproducibility (Pearson's $r = 0.92\text{--}0.97$ over 24 comparisons; Figure S1C) and were merged for subsequent plots and analyses to increase sample size. The absolute loop frequency within each of the demultiplexed treatment conditions showed good agreement with Hi-C data from earlier studies degrading CTCF¹ or cohesin,⁴ both in qualitative features (Figures 1C and 1D) and Pearson's correlation (Pearson's $r = 0.8\text{--}0.93$; Figure S1D).

We next asked how these distinctive population average loop frequencies (Figures 1C and 1D) manifest at the single-cell level. We began with an unbiased clustering approach, using t-distributed stochastic neighbor embedding (t-SNE) analysis to cluster the single-chromosome pairwise distance matrices. This produced a well-connected single cloud (Figure 1E). Despite clear differences among the induced degradation conditions and untreated cells at the population average, individual traces from these populations stretched across the cloud, overlapping one another substantially (Figure 1E). Traces from cohesin-depleted cells showed the most asymmetric pattern (Figure 1E). These observations parallel our recently reported finding that the SOX9 locus shows distinct patterns of TADs, sub-TADs, and stripes in ESCs compared with differentiated cranial neural crest and yet produces overlapping clouds in dimensionality reduction.¹⁷

To test how these results compare with current predictions of single-cell variability, we applied t-SNE to polymers produced from Langevin dynamic simulations of loop extrusion^{6,18} using the open2c polychrom toolbox¹⁹ derived from earlier works^{6,18} (**STAR Methods**). Considerable evidence supports the model that cohesin shapes genome structure, including TADs, through

loop extrusion (for review see Mirny and Dekker⁸ and Davidson and Peters²⁰). In this model, cohesin is loaded onto DNA and extrudes a loop until it is stalled by CTCF. As expected,⁶ simulations including cohesin and CTCF formed TADs between CTCF boundaries and loop-dots between convergent CTCF sites, whereas simulations without CTCF or cohesin did not (Figure 1F). t-SNE analysis of simulated polymers spanning a few TADs, much like our data, revealed overlapping clouds for polymers with or without CTCF or cohesin (Figure 1F).

Thus, both our multiplexed ORCA data and simulations support the idea that TADs are population-level features that arise from a continuous and dynamic process and do not correspond to physical and static structures in single cells. We conclude that dimensionality reduction approaches such as t-SNE, popularized in their ability to distinguish discrete cell populations marked by unique gene combinations, may not be ideal tools to highlight differences in continuum processes such as the folding of individual chromatin polymers.

CTCF and cohesin affect loop density and 3D separation

To complement the unweighted dimensionality reduction of traces, we next focused on features of particular interest, starting with loops in single-chromosome traces. To facilitate the interpretation of 3D traces projected into a 2D page, we assigned distinct colors to each looped region, whereas non-looped regions were colored in gray (Figure 2A). Traces from cells without CTCF (Figure 2A), were indistinguishable by eye in terms of looping from NT traces. By contrast, traces from cells without cohesin showed fewer loops (e.g., Figure 2B).

To quantify these effects, we computed the difference in loop frequencies between +Aux and NT cells (Figures 2C and 2D for CTCF and RAD21, respectively). When such subtractions of contact maps are performed with Hi-C data, the separate normalizations applied to each condition (to reduce sequencing artifacts) may bias the magnitude and sign of the subtraction map. This is not a concern for our loop maps, which do not require normalization such as matrix balancing.

For CTCF depletion, subtraction maps showed gains in some regions, largely balanced by losses elsewhere (Figures 2C and S2A), consistent with the visual impression from single traces of similar loop numbers (Figure 2A). Loop gains were significantly enriched at between-TAD regions (Figure 2E, Binomial statistic $p = 4.5\text{e}{-}11$ and $p = 1.12\text{e}{-}7$ for the regions of chromosome 6 and chromosome 3, respectively), consistent with previous observations from Hi-C and microscopy.^{1,9,10} In contrast to prior work, however, which concluded CTCF has little role in within-TAD cohesion compared with TAD separation,^{1,10} we saw a marked and significant loss of loops from within-TAD regions (Figures 2C and 2F, $p = 2.34\text{e}{-}7$ and $p = 7.85\text{e}{-}7$ Wilcoxon-signed rank sum, for the regions of chromosome 6 and chromosome 3, respectively). Subtraction of 3D distance showed that the loss of loops within TADs led to slight decompaction within TADs (Figures 2G and 2H). Notably, loop loss within TADs was observed in published Hi-C data, but it was suggested at the time to be a normalization artifact.¹ This justified interpretation rested on both consideration for the issues in Hi-C matrix balancing and subtraction, mentioned above, and an inability to detect the effect by concurrent analysis with FISH.¹

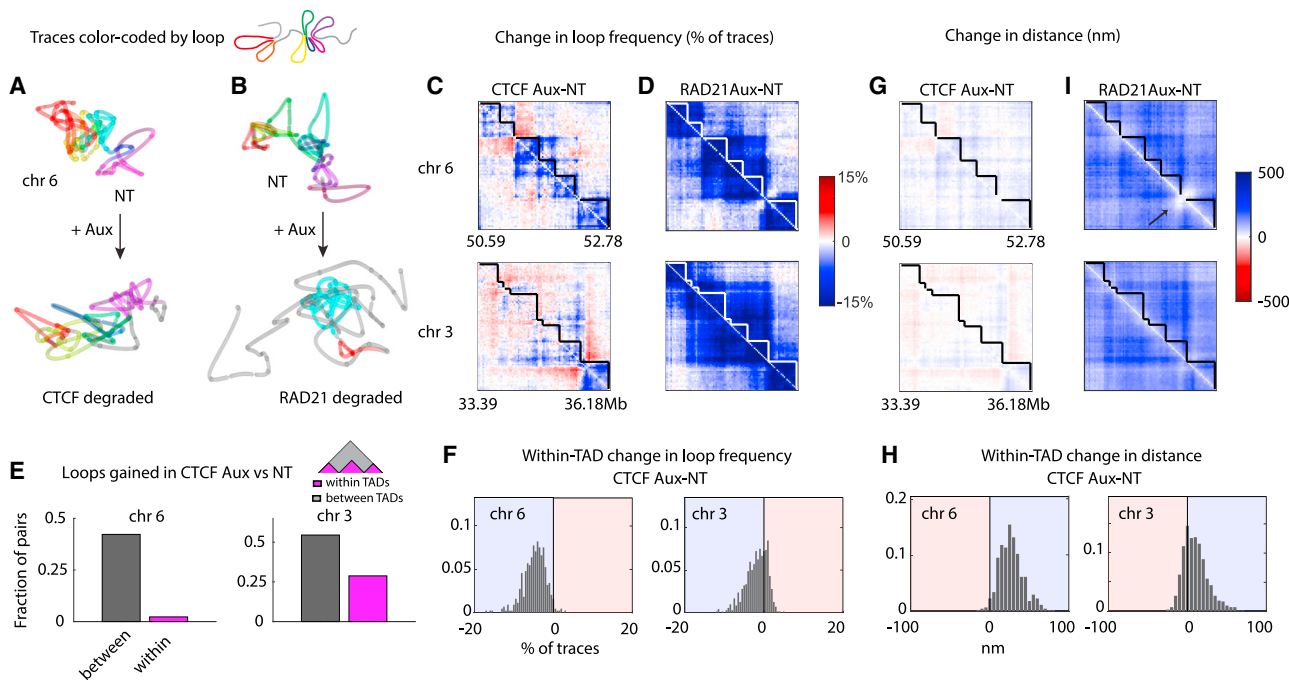


Figure 2. CTCF and cohesin affect loops and 3D distances

(A and B) Example single chromosome traces from untreated (NT) and auxin-treated cells depleting either CTCF (A) or cohesin (B) color coded by loop and where regions that are not in loops are colored in gray. Tube radius is 15 nm, and sphere radius is 20 nm.

(C and D) Differences in loop frequency between NT and CTCF-depleted (C) or cohesin-depleted cells (D).

(E) Quantification of fraction within or between TAD regions that gained loops on CTCF depletion.

(F) Distribution of changes in loop frequency within TADs between CTCF NT and CTCF +Aux conditions.

(G) Differences in median distance between NT and CTCF-depleted conditions.

(H) Distribution of distance differences within TADs between CTCF NT and CTCF +Aux conditions.

(I) Differences in median distance between NT and cohesin-depleted conditions.

Understanding this loss of loops within TADs is thus an interesting observation to try to explain with future models.

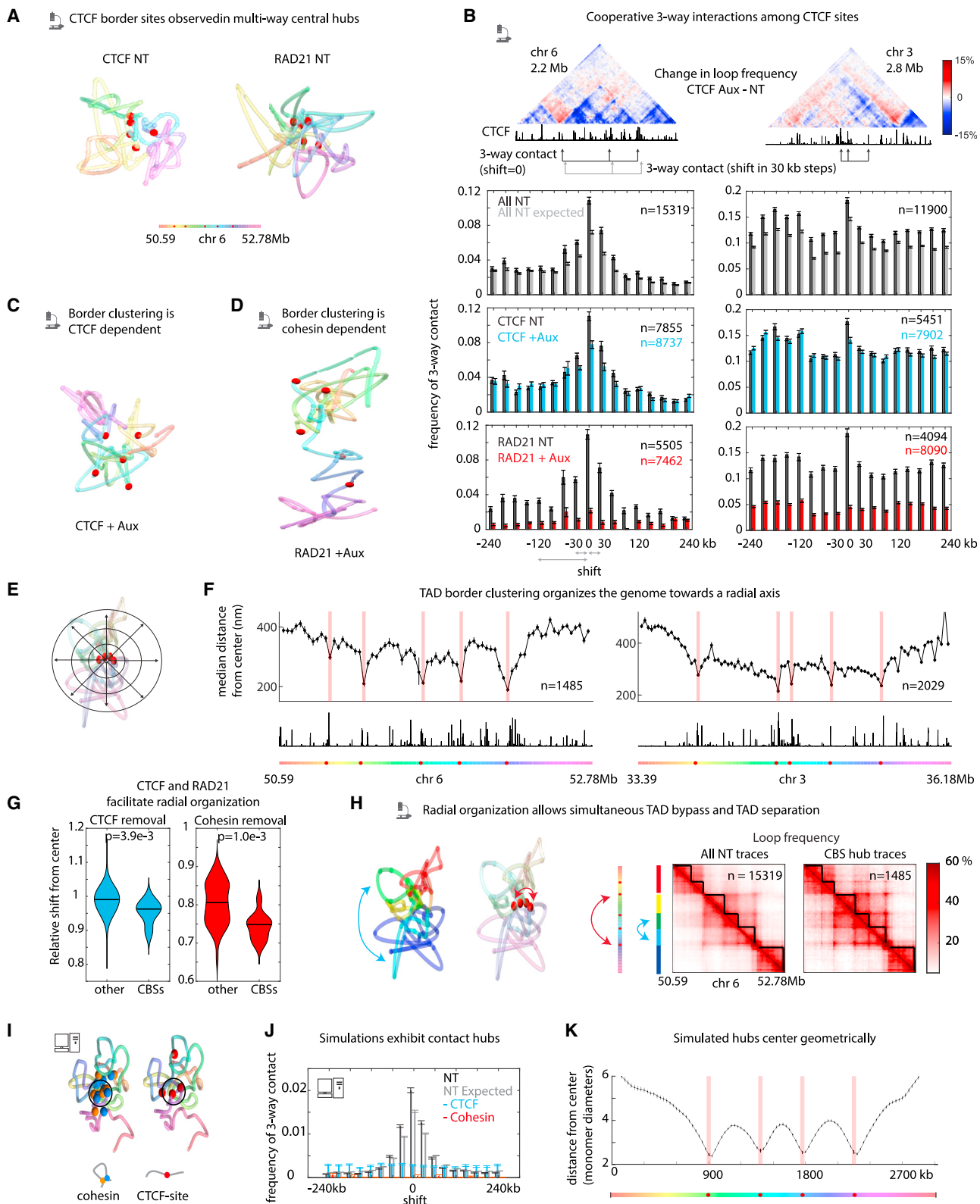
Contrasting the mixed gain and loss of loops on CTCF removal, cohesin removal reduced loops generally (Figures 2D and S2B). Subtraction of 3D distance showed more substantial and significant ($p < 0.05$ Wilcoxon rank sum) global expansion than CTCF both within and between TADs (Figures 2I and S2C–S2E), consistent with visual impression from single-chromosome traces (Figure 2B). Despite the fact that cohesin-depleted cells lack TAD boundaries (Figure 1), the regions between neighboring TADs were bridged by fewer cross-TAD loops (Figure 2D) and physically more distal (Figure 2I). Thus, loss of TADs is not caused by increased cross-TAD contacts but rather an overall expansion of distances within and between TADs. Our data also resolve the conflicting super-resolution data described above: the loss of loops between TADs matches the decrease in TAD overlap reported by Luppino et al.⁹ and the expansion in volume is consistent with measurements by Szabo et al.¹⁰

To test whether the expansion upon the depletion of cohesin was dependent in part or in full on the loss of sister chromatid cohesion, we performed immunofluorescence labeling of Geminin and ORCA in the same cells (Figure S2F). Geminin is a cell-cycle-regulated protein that is not detected in G1 and progressively accumulates through the S and G2 phases of the cell

cycle. We selected cells with low Geminin levels (lowest 25% of the cells) and found that these also showed expansion upon loss of cohesin, both within and between TADs (Figure S2G). Furthermore, we found no correlation between Geminin levels and the median pairwise separation among all imaged domains on a single-cell basis (Figure S2H), and there was not an obvious separation of G1 or G2 cells in the t-SNE analysis (Figure S2I). From this, we conclude that the expansion of chromosomes in cells without cohesin is primarily driven by changes in the *cis*-structure and not the loss of sister cohesion.

Multi-way contacts between loop anchors depend on CTCF and cohesin

Having examined changes in the loop frequency and the 3D distance in a pairwise fashion, we next turned to the analysis of multi-way contacts. Visual inspection of traces revealed that loops often shared common anchor points (Figure 3A). We noticed a tendency to find CTCF boundary sites (CBSs) clustered at these loop bases (Figure 3A). To quantify this we computed the frequency of three-way contacts among CBSs across all traces. We compared these with the distance-matched, non-CBS contacts using a sliding window across the genomic regions. We found that three-way contacts among CBSs were more common than expected based on the measured pairwise contact frequencies (assuming pairs are



(legend on next page)

independent) (Figure 3B, black as compared to gray bars) and higher than for non-CBS triplets (Figure 3B). Depletion of CTCF significantly reduced the frequency of three-way contacts among both CBSs and CBS-proximal sites, although made little changes for CBS-distal sites (Figures 3B, blue bars and 3C). Degradation of cohesin clearly reduced the preference for CBSs and CBS-proximal regions to form three-way contacts (Figures 3B, red bars and 3D).

In addition to clustering, we found chromosome traces tended to organize in a radial pattern, in which the CBS hub was positioned in the geometric center of the trace (Figure 3E). Quantifying the traces which contained CBS hubs (17%–20% of traces) of at least 3 sites (out of 5 CBSs in the regions from chromosome 6 or chromosome 3), CBSs were clearly displaced toward the center relative to flanking regions (Figure 3F). Depletion of CTCF or cohesin significantly reduced the tendency for central positioning of these sites (Figure 3G, $p < 0.01$ Wilcoxon rank sum). This suggests that cohesin may drive the centering of CTCF, possibly through the formation of loops that sterically distribute around the hub forming a rosette structure.

Furthermore, we found this rosette organization supports TAD-boundary function concurrent with cross-TAD hub formation. In individual traces, 1 Mb distal CBSs exhibited 3D proximity even while maintaining separation between intervening elements (Figure 3H). At the population level, TAD boundaries in hub-containing traces remained as clearly visible as in the bulk population, despite the cross-TAD interaction needed for hub formation (Figures 3H, S3A, and S3B).

In the dimensionality reduction of traces using t-SNE, hub-containing traces were distributed across the map (Figure S3C), reinforcing our earlier observation of the limitations of that approach for identifying patterns in single-chromosome folding.

To understand how cohesin loop extrusion may influence the preferential three-way interaction among CBSs and their positioning in the center of the domain, we returned to simulations. With sufficient density/lifetime of extruders, we observed collisions among extruders, leading to stacking of cohesin-mediated loops (Figure 3I, left). Steric effects among the loop arms encouraged the loop bases to collect in the geometric center. As extrusion blockers (CTCF) spend more time at loop bases than other sequences, these sites are more commonly found in the resulting

multi-way hubs (Figure 3I [right] and Figure 3J) and also centered (Figure 3K). Thus, loop extrusion can explain CBS clustering which is CTCF and cohesin dependent, geometrically centered, and not dependent on assuming adhesive interactions among CTCFs.

For the chromosome 6 region, we observed that the two strongest borders were closely linked not only to CTCF sites but also to Polycomb (Pc) domains. One of the domains spans the ~100 kb, CTCF-rich, Pc-bound *Hoxa* gene cluster. We note that this Pc-coated domain was the only non-significantly changed region, remaining contracted on cohesin depletion (Figures 2I and S2E, arrow). The second Pc domain marks the CTCF-bordered, *Hox*-regulatory region, ~1 Mb distal from the *Hox* cluster.^{21–23} The two Pc regions loop together in NT cells at a higher frequency than flanking regions (Figure S3D, arrow). Upon cohesin depletion, this local enhancement in looping frequency between the Pc-bound regions is still detected in the ORCA data, although at reduced strength compared with NT cells (25% of the cells relative to 37% in RAD21 NT cells), suggesting it is a Pc-dependent interaction. To further test this, we used dTag13 inducible protein degradation to deplete endogenous proteins EED and Ring1b, core subunits of the two major Pc repression complexes^{24,25} (Figure S3E). Similar to cohesin depletion, Pc depletion resulted in a reduction of the loop frequency (Figures S3F and S3G), the three-way contact frequency between CBSs (Figure S3H) and reduced central positioning of those sites (Figure S3I). In contrast to cohesin depletion (Figure 2I), 3D distance subtraction showed that Pc loss had the strongest effect for regions outside the Pc loop (Figure S3J), highlighting a difference in the mechanism by which they affect loop frequency. Together, these observations suggest that for this domain, Pc-Pc interactions cooperate with cohesin to facilitate long-range loop-dots and multi-way contacts, rather than opposing them.

Cohesin loss has distinct effects across genomic scales

We next asked whether disrupting the loop frequency by depleting cohesin at the TAD scale had an effect on the chromatin structure at larger genomic scales. We designed probes spanning both a ~30 Mb region and the whole chromosome (~150 Mb) for both chromosomes 6 and 3 (Figure 4A).

Figure 3. Loop stacking promotes clustering of loop anchors and separation between TADs

- (A) Examples of single chromosomes from NT cells with CBSs colored in red. Tube radius is 15 nm, and sphere radius is 20 nm except for readouts corresponding to CBSs are represented as spheres of 30 nm radius.
- (B) Top panels, loop frequency difference map between CTCF Aux and NT cells, with arrows indicating the positions chosen for the three-way contact analysis. Lower panels: frequency of three-way contact between the three CTCF-marked positions indicated by black arrows computed over all NT cells. Frequency of three-way contact for other distance-matched triplets (black) is shown as a function of how far (in kb) they are shifted from the black triplet. In gray, expected three-way contact based on the pairwise contact probabilities; in blue and red are the frequencies of three-way contact for CTCF +Aux and RAD21 +Aux conditions, respectively. Error bars show 95% confidence intervals.
- (C and D) (C) Example chromosome trace for CTCF +Aux and (D) RAD21 +Aux conditions. Tube radius is 15 nm, and sphere radius is 20 nm except for readouts corresponding to CBSs are represented as spheres of 30 nm radius.
- (E) Schematic of radial organization of loops, with CBSs at the center.
- (F) Quantification of positions for each readout relative to the geometric center of the trace. Error Bars show 95% confidence intervals. Red bars indicate positions corresponding to CBSs.
- (G) Fold change in central positioning upon CTCF or cohesin depletion for CBSs relative to other readouts for chr6 and chr3 combined.
- (H) Chromosome trace, colored by TAD, illustrating a radial organization with clustering of CBSs and separation of TADs (left). Loop frequency for cells containing CBS hubs shows clear TAD boundaries.
- (I–K) (I) Simulated polymer traces with visualization of cohesin or CBSs illustrate how clash of loops can drive multi-way contacts between CBSs (J) and lead to central positioning of these CBSs (K).

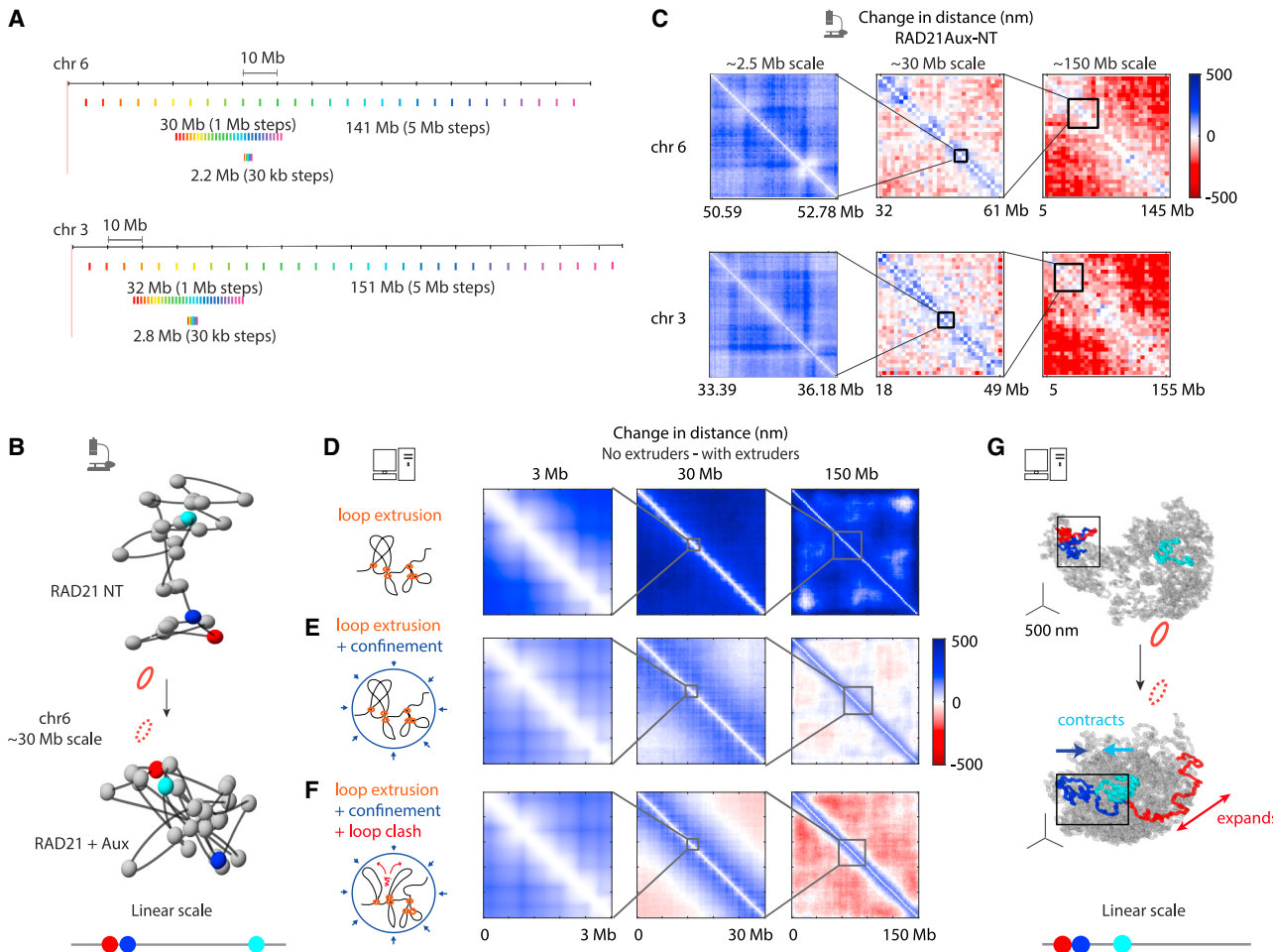


Figure 4. Cohesin loss leads to increased mixing at the chromosome scale

(A) Schematic of probes designed to image folding of ~ 30 and ~ 150 Mb regions of the genome, shown relative to the ~ 2.5 Mb probes imaged previously. (B) Example of single chromosome traces for ~ 30 Mb with or without cohesin. Readouts that correspond to consecutive probes (1 Mb apart) are marked by red and blue spheres, whereas a more distal readout (20 Mb away) is labeled in cyan. Tube radius is 15 nm, and sphere radius is 100 nm. (C) Differences in median distance between RAD21 NT and RAD21 + Aux cells for the ~ 2.5 , ~ 30 , and ~ 150 Mb regions. (D–F) Median distance difference maps for simulations with or without loop extrusion factors at different scales for simulations. Simulations were run with: loop extrusion only (D); loop extrusion and low-density confinement (E); and loop extrusion, low-density confinement and decreased strand crossing (F). (G) Simulated chromosome trace at the chromosome scale (150 Mb) with or without loop extrusion factors from simulations in (F). The chromosome is shown in gray. Other chromosomes inside the simulated nucleus are not shown to avoid overlap. Individual 3 Mb domains are colored. Their positions on the linear polymer are indicated by the color bar.

At these larger spatial scales, we observed that consecutive probes could be found farther apart following cohesin depletion (Figures 4B and S4A, red and blue highlighted steps), consistent with our observations at the ~ 2.5 Mb scale (Figure 3H). However, this increased separation did not propagate to larger length scales. More distal regions we examined often appeared closer after cohesin depletion, such as the 20 Mb-separated loci shown in Figure 4B (red and cyan) or the 100 Mb-separated loci in Figure S4A (red and cyan). We quantified this by plotting the change in median pairwise distance (Figure S4B) among all points at both scales (Figure 4C). While pairwise distances less than ~ 4 Mb apart increased significantly (Figures 4C and S4C), beyond the ~ 4 Mb separation, we found a gradual transition to decreased distance (Figure 4C, blue to white to red). The

decrease in distance became more pronounced and statistically significant as a function of linear separation (Figures 4C and S4B).

To understand the mechanisms behind the multi-scale effects of cohesin removal, we performed polymer simulations. We asked which, if any, parameter choices within the loop extrusion modeling framework could recapitulate our results. Adding cohesin-extruded loops to simulated chromosomes generally contracted the chromosome across all scales (Figure 4D), consistent with prior conclusions modeling mitotic and interphase chromosomes,^{8,18} although contrasting our observations above. We next hypothesized that nuclear crowding may induce the chromatin polymer to fold back on itself more in the absence of cohesin. Simulated chromosomes confined in a hard sphere, such

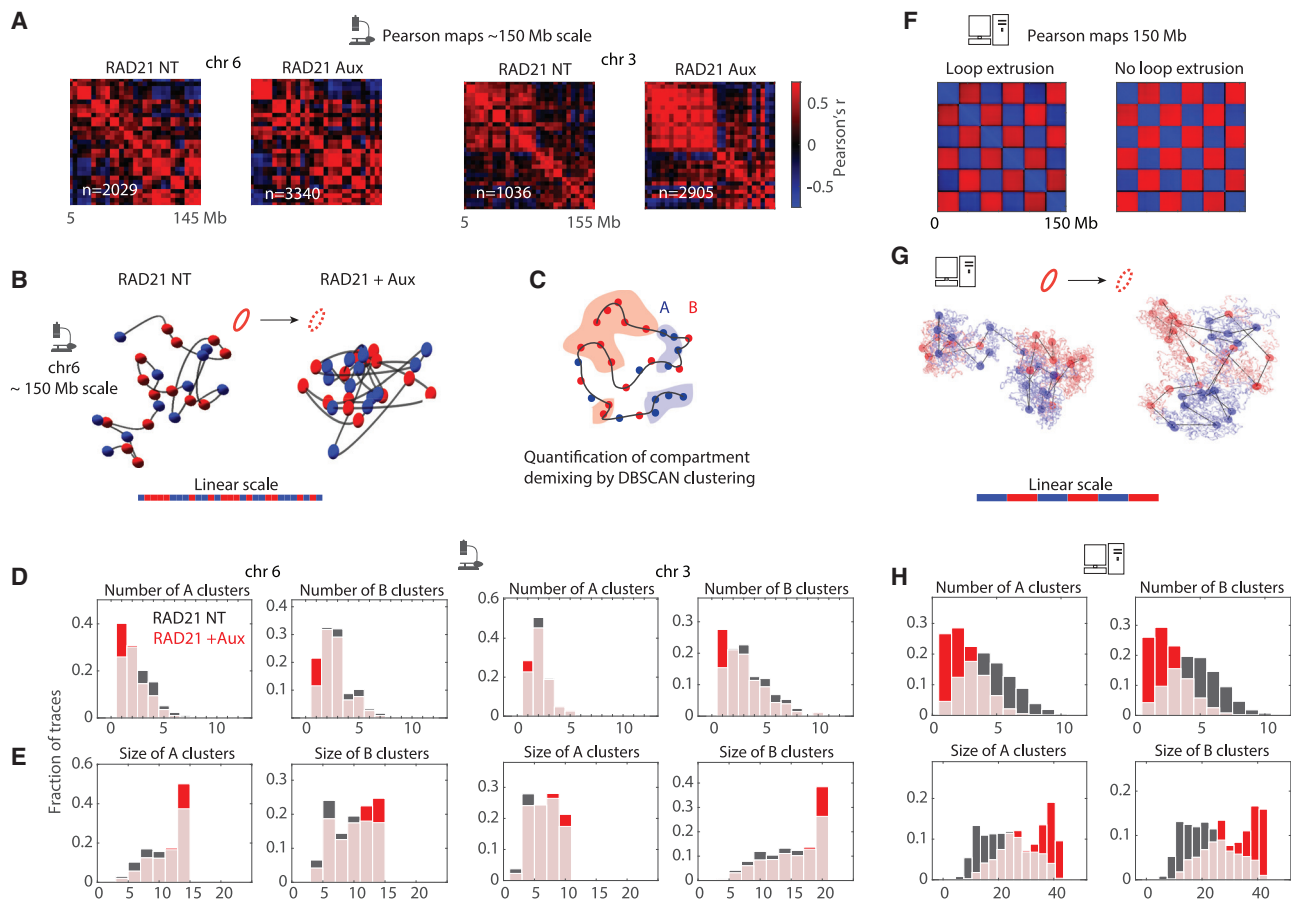


Figure 5. Compartments strengthen after cohesin loss but remain heterogeneous in single cells

(A) ORCA Pearson correlation maps for the 150-Mb scale probes in RAD21 untreated or RAD21 +Aux cells.

(B) Example chromosome traces from RAD21 NT or RAD21 +Aux cells colored by compartment identity. Tube radius is 15 nm, and sphere radius is 100 nm.

(C) Schematic of compartment clustering by DBSCAN.

(D) and (E) Distributions of compartment cluster number (D) and cluster size (E) for 150 Mb domains from the ORCA data quantified by DBSCAN. Cluster size corresponds to the number of barcodes. Black for NT, red for RAD21 +Aux, and light pink for the overlapping regions.

(F) Pearson maps for simulated polymers.

(G) Example chromosome traces from simulations with or without loop extrusion.

(H) Distributions of compartment cluster number and cluster size for simulations with or without loop extrusion of 150 Mb simulated polymers quantified by DBSCAN.

that the polymer accounted for 20% of the internal volume, showed expansion at short length scales, but little systematic change in 3D distances at larger genomic scales (Figure 4E). Importantly, these simulations allowed for only a limited degree of steric interactions among loops, a feature intended to capture the ability of abundant topoisomerases to facilitate strand-crossing events.¹⁹ In our third simulation, we reduced the probability of such crossing, allowing more steric clash between cohesin-induced loops. In these simulations, we finally reproduced the switch from expansion to contraction, with a cross-over point on the scale of tens of cohesin loops (~4 Mb) (Figures 4F and 4G). This finding parallels recent polymer theory showing that chromatin loops “experience topological repulsion.”²⁶

Our ORCA measurements and simulations both show that cohesin loops are not only important to give rise to TADs but are

also required for the maintenance of a stiffer, more ordered chromosome structure at the whole chromosome scale (Figure 4C).

Previous work using Hi-C found that the depletion of cohesins led to a slight strengthening of compartments.^{2,4,27} Compartments refer to a plaid pattern commonly seen at the chromosome scale in Hi-C contact maps, indicating a preferential separation of the genome into two groups, commonly denoted A and B.²⁸ The separation is readily visualized through the Pearson map, where each element of the map reports the cross-correlation of the corresponding row and column after distance normalization.²⁸ Examining the Pearson maps for the 30 Mb and full-chromosome ORCA data, we observed a similar plaid pattern to Hi-C from mESCs, which also strengthened on cohesin depletion (Figures 5A and S5A–S5D).

To determine to what extent this compartment strengthening is reflected on a cell-to-cell basis, we colored each chromosome

trace by its A/B compartment designation (Figure 5B; Table S3). Despite the clear plaid pattern in the Pearson maps (Figure 5A), individual cells showed little evident demixing of A/B chromatin. To quantify this effect, we used density-based spatial clustering applications with noise (DBSCAN) to identify A-A and B-B clusters within each trace (Figure 5C). As a metric of A/B demixing, we quantified the number of clusters and the size of the largest cluster (Figures 5D and 5E) in each trace. We found a median of 3–4 clusters for both A and B chromatin, indicating these chromosomes are not fully demixed into A/B types. On cohesin depletion, the distribution of the number of clusters shifted to the left (fewer clusters) and the distribution of cluster size shifted to the right (bigger clusters) indicating more demixing (Figures 5D and 5E). Polymer simulations incorporating an alternating pattern of weak sticky interactions, along with the aforementioned loop extrusion, confinement, and clash, were able to reproduce a strong plaid pattern at the population level while lacking clear demixing at the single trace level (Figures 5F and 5G). Removal of loop extrusion from the simulations resulted in a mild strengthening of the plaid pattern (as shown previously¹⁸) and a mild increase in demixing at the single trace level (Figures 5F–5H).

The lack of clear compartmentalization in ESCs on a cell-by-cell basis is consistent with previous observations from electron microscopy²⁹ and high-throughput FISH³⁰ and contrasts the spatial separation of compartments observed by chromosome tracing in more differentiated fibroblasts.³¹

Thus, at the single trace level, we see that the clear compartment signal (Pearson map) does not necessarily correspond with visually apparent demixing in single chromosomes. At the population level, the increase in compartments' strength upon cohesin removal appears to be a consequence of the decreased distance between distal (>4 Mb) sites. By promoting a small number of local interactions (<4 Mb contacts) while inhibiting a large selection of potential distal interactions (>4 Mb contacts), cohesin tends to oppose compartmentalization primarily because most “checks” in the plaid require the formation of distal contacts (>4 Mb). Thus, our observation of the distance change upon cohesin depletion provides a new explanation of the established observation of compartment strengthening on cohesin removal.

Cohesin depletion increases the entropy in genome folding and variability in gene expression

To better quantify the disorder in genome folding observed across genomic scales, we next computed the change in the entropy of the ensemble of traces upon depletion of cohesin or CTCF. A highly ordered folding pattern is expected to have a more narrow distribution of 3D distances between equally spaced points along the trace. Whether these steps are large or small, a narrow distribution will have a smaller entropy (Figure 6A). In contrast, a heterogeneous ensemble of traces will have a broad distribution and larger entropy (Figure 6A). We computed the entropy of the distance distribution from each viewpoint along the trace across all of our data and plotted the change in this value on CTCF or cohesin removal (Figure 6B; STAR Methods). Cohesin depletion led to increased entropy at all scales relative to NT cells. By contrast, CTCF-depleted cells

showed more modest changes in entropy at the ~2.5 Mb scale and little change at the ~30 Mb or chromosome scale (Figure 6B).

Previous studies have shown that degradation of cohesin has a limited immediate effect on transcription^{2,4,32–34} relative to degradation of transcription factors or cofactors^{24,35–37} or genetic disruptions of TAD borders.^{15,38–41} Given the increased entropy in the genome structure, we wondered whether cells would exhibit increased variability in gene expression.

We performed multiplexed single-molecule RNA FISH to measure the expression of a set of developmentally regulated pluripotency genes. We used cellular barcoding to minimize batch effects among different treatment conditions and cell lines (RAD21-AID ± Aux, CTCF-AID ± Aux, and E14) (Figure 6C). We also added mock (DMSO) treated cells for each genetic background as a further comparison. The mean mRNA counts showed small fold changes between treatment conditions, scarcely stronger than for our mock treatment (Figure 6D). However, we found that most genes tested showed a statistically significant, moderate increase in the coefficient of variation (COV) after cohesin depletion (Figure 6E). Depletion of CTCF had less effect on the COV (Figure 6E), likely reflecting fewer changes in the genome structure (Figures 2G vs. 2I, S2C vs. S2D, and S6A–S6C) and entropy (Figure 6B).

Cluster analysis of RNA FISH data by t-SNE showed that cohesin-depleted cells did not split into distinct groups nor cluster separately from NT cells (Figure 6F). This suggests that increased variability was not due to partial differentiation of the mESCs after auxin treatment for 4 h. Indeed, all the genetic backgrounds and treatment conditions clustered together (Figure 6F), with variation of cell-cycle-dependent factors aligning with one major t-SNE axis and variation in *Tbx3* defining the other.

Overall, our data show that acute loss of cohesin leads to disordered chromosome structures with higher entropy across genomic scales, ranging from a few Mb to whole chromosome, and leads to modestly increased cell-to-cell variability in gene expression, which is missed by bulk population assays.

DISCUSSION

Here, we introduced a multiplexed approach for ORCA, enabling simultaneous measurement of chromosome folding across multiple treatment conditions and cell backgrounds, substantially enhancing the experimental throughput. Our approach enables quantification of the physical structure in absolute units, enabling quantitative comparison between conditions, overcoming a limitation of Hi-C. As the field moves increasingly to the study of perturbations, we expect the ability to measure absolute frequency differences across genomic length scales without normalization artifacts or batch effects, the ability to measure variation in single cells, and the ability to process multiple conditions at a time will facilitate more rapid understanding. In this work, we characterized the structure of the interphase genome, expanding our understanding of the role of CTCF and cohesin in shaping that structure beyond their previously recognized roles in TAD formation and identifying new implications for gene regulation.

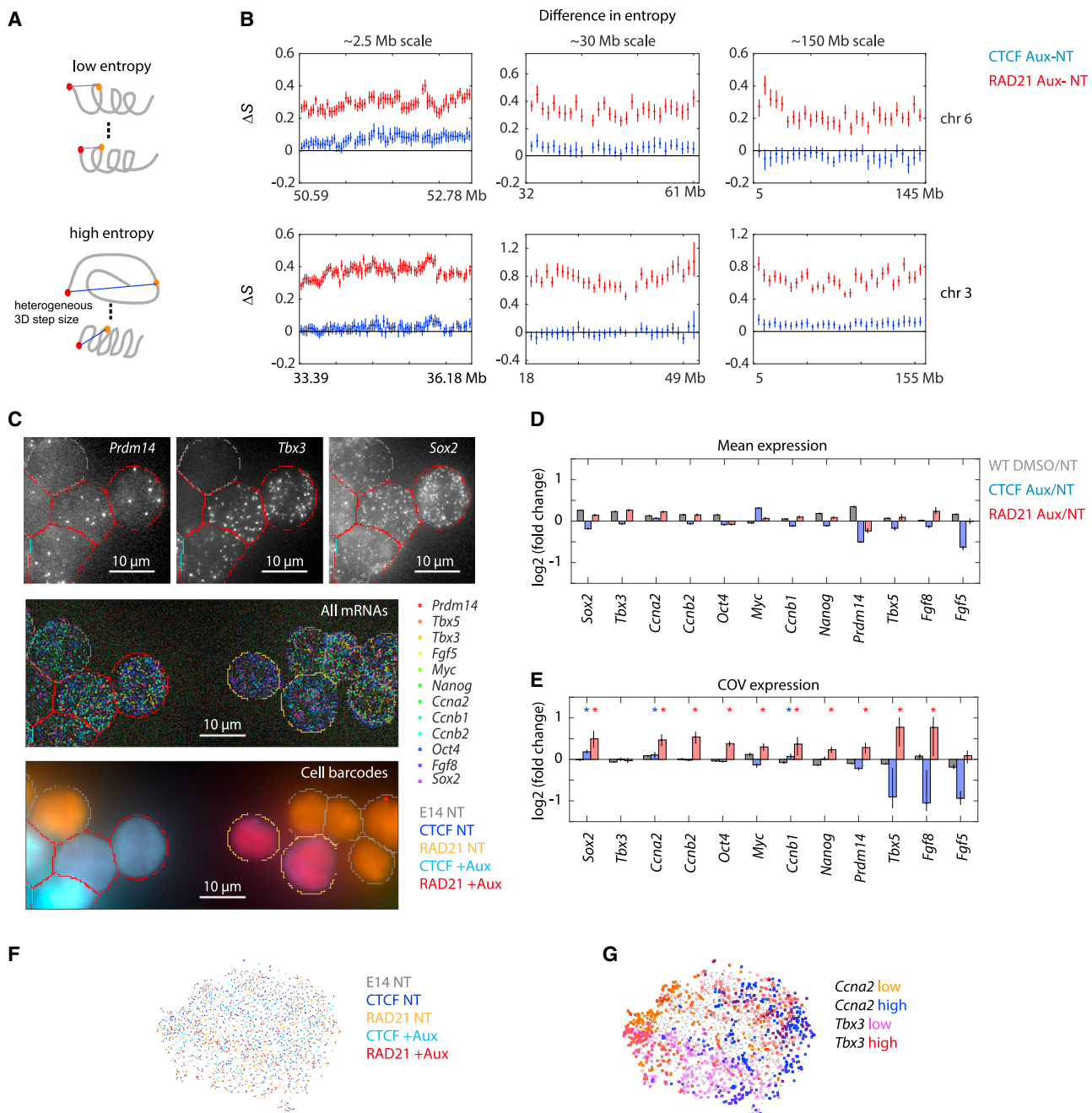


Figure 6. Cohesin depletion increases the entropy in genome folding and variability in gene expression

(A) Schematic illustrating an ordered (top) and a disordered (bottom) polymer and consequences for distance between two points on the polymer (in red and orange).

(B) Difference in entropy per barcode between CTCF +Aux or RAD21 +Aux and NT cells.

(C) Example of multiplexed cells for different treatment conditions labeled by single-molecule FISH. Top row: individual mRNAs, middle row: 12 mRNAs in the experiment, bottom row: cell barcode labels. Colors of cell outlines correspond to the treatment conditions determined from demultiplexing cell barcodes.

(D) Mean fold change of expression.

(E) Fold change in coefficient of variation (COV) where * denotes $p < 0.05$ (Kolmogorov-Smirnov test).

(F) t-SNE analysis of mRNA expression, color coded by treatment condition.

(G) t-SNE plot color coded by the expression level of *Tbx3* or *Ccna2*.

Together, our multi-scale experiments and simulations suggest that cohesin and CTCF organize the genome through their distinct effects on chromatin loops and loop stacking (Figure 7). Cohesin increases the density of chromatin loops, and thus, proximal sequences (<4 Mb) are brought into frequent contact, whereas distal (>4 Mb) sequences are held apart by the clash of many loops. When cohesin molecules collide, the loops formed by cohesin stack together. Loop bases aggregate into a central hub, and steric effects among the projected loops drive the hub into the geometric center. As CTCF-border sites (CBSs) are more likely to be at the base of cohesin loops than other sequences, this process also positions CBSs in a hub at the domain center, creating a “rosette.” This model explains the observed high-frequency multi-way contact among CBSs and their position in the domain center and explains the dependence of both behaviors on CTCF and cohesin. The experimentally observed rosette structure meanwhile explains how CTCF-proximal regions can bypass intervening CTCF-borders to contact more distal, CTCF-linked regions, without abrogating the boundary behavior of the intervening sites (discussed more below) (Figure 7A).

This radial organization of chromatin around a central hub of CTCF provides evidence for a long hypothesized “chromatin rosette” model, primarily motivated by pairwise 3C data^{42–46} (reviewed in Labrador and Corces,⁴⁷ Phillips and Corces,⁴⁸ and Gómez-Díaz and Corces⁴⁹). This model has since been challenged by some genetic analyses⁵⁰ and conflicting results from multicontact Hi-C data regarding multi-way interactions among CBSs.^{11,51} We reconcile these conflicting views by super-resolution imaging of CTCF-rosette-structures in intact nuclei. We also find them to be rare in a given population snapshot (~17%–20%) and thus likely transient. Although previous work hypothesizing rosettes emphasized their potential role in multi-enhancer or multi-gene hubs, we find rosettes also play a role in maintaining TAD boundaries.

This rosette organization has important implications for *cis*-regulatory interactions. The first is a mechanism for TAD-border bypass, which arises from the formation of the CBS hubs. *Cis*-regulatory elements proximal to CBSs sites will make more frequent contact with CBS-proximal promoters, even if separated by TAD borders (Figure 7A). Additional promoters in this domain that are not near a CBS, even if they are linearly closer to the enhancer in the genome sequence, are more likely to be radially extruded outside the hub. Thus, this structure provides a potential explanation for both boundary-bypassing enhancers and promoter-skipping enhancers (Figure 7A). It has been shown that *Hoxa* genes respond to developmental enhancers positioned near the CBS 1 Mb upstream of the *Hoxa* locus, on the far side of several unrelated genes and two prominent TAD boundaries.^{23,52} The updated rosette model provides a simple explanation of how this enhancer might use a chain of cohesin-dependent loops to reach the *Hoxa* genes, without ectopically activating the intervening promoters (Figure 7A). We recently found a similar configuration at the *Pitx1* locus in developing mouse limbs, another important developmental control gene.⁵³ The rosette organization also suggests that it will be difficult to disrupt E-P interactions by inserting new CTCF-insulators between them if the enhancers and promoters are themselves CTCF bound or CBS proximal. Interestingly, the *Sox2* promoter

and its mESC enhancer are both CTCF bound, and two groups who independently inserted CTCF sites between these found that it failed to efficiently block E-P communication, despite establishing a new TAD border.^{54,55}

The second implication of loop stacking is that it could protect genes from ectopic regulatory contacts with the rest of the genome (Figure 7B). Although the probability of a gene ectopically encountering any particular enhancer >4 Mb is extremely low, the total number of such potential ectopic encounters, across all enhancers >4 Mb is considerable. By significantly increasing the separation from all elements of the chromosome >4 Mb apart, cohesin reduces the potential for any ectopic enhancer-promoter interactions. With this perspective, rather than expecting a global up- or down-regulation of genes after the depletion of cohesin, our ORCA measurements suggested that each gene and each cell may behave differently. This would manifest as increased cell-cell variation in mRNA levels, which we observed for most of the developmentally important genes we assayed by single-molecule RNA FISH. Recent studies have similarly reported that disruptions affecting the population-level 3D chromatin organization increase variability in gene expression, using single-cell RNA-seq,⁵⁶ RNA-FISH and flow-cytometry,⁵⁷ or integrative modeling of omics data.⁵⁸ We build on this result by directly linking the structural heterogeneity (entropy) in chromatin folding (greater for cohesin depletion than CTCF) to the expression heterogeneity in the same cells (greater for cohesin depletion than CTCF). Whether and how these acute changes in cell-cell variability due to disruption of the chromatin structure connect to functional outcomes of cohesin loss or reduction in development and disease^{59–64} will require future investigation.

The structural changes we observed in genome organization at the chromosome scale also allowed us to revisit recent conclusions about the role of cohesin in aspects of genome organization, such as compartments and Pc loops. It has been proposed that cohesin opposes demixing of the genome into A/B compartments directly through its ability to bridge compartment boundaries and pull together A and B chromatin.^{2,18,27} This proposal is supported by the observed strengthening of A/B compartments upon cohesin depletion.^{2,27} Our data suggest an additional mechanism. By significantly decreasing the frequency of interactions >4 Mb, through the dense stacking and clash of loops, cohesin indirectly disrupts compartmentalization by reducing the opportunity of linearly separated A or B domains to contact and mix (Figure 7B).

It has been proposed that cohesin processivity can disrupt the Pc homotypic interactions that drive the formation of ultra-long range contacts among Pc domains (1–20+ Mb), “Pc loops.”⁴ These data are supported by the observation that these loops strengthen upon cohesin degradation.⁴ Such Pc loops are proposed to be important for Pc-spreading and epigenetic maintenance.^{65–67} As we have shown for the 1-Mb scale interaction in the *Hoxa* region, the shorter Pc-Pc interactions actually decrease in absolute frequency upon cohesin loss, whereas >4 Mb interactions increase along the entire chromosome. Thus, the effect of cohesin on Pc loops we propose is also an indirect effect of cohesin “linearizing” the chromosome (promoting short <4 Mb contacts and reducing longer range ones). Indeed,

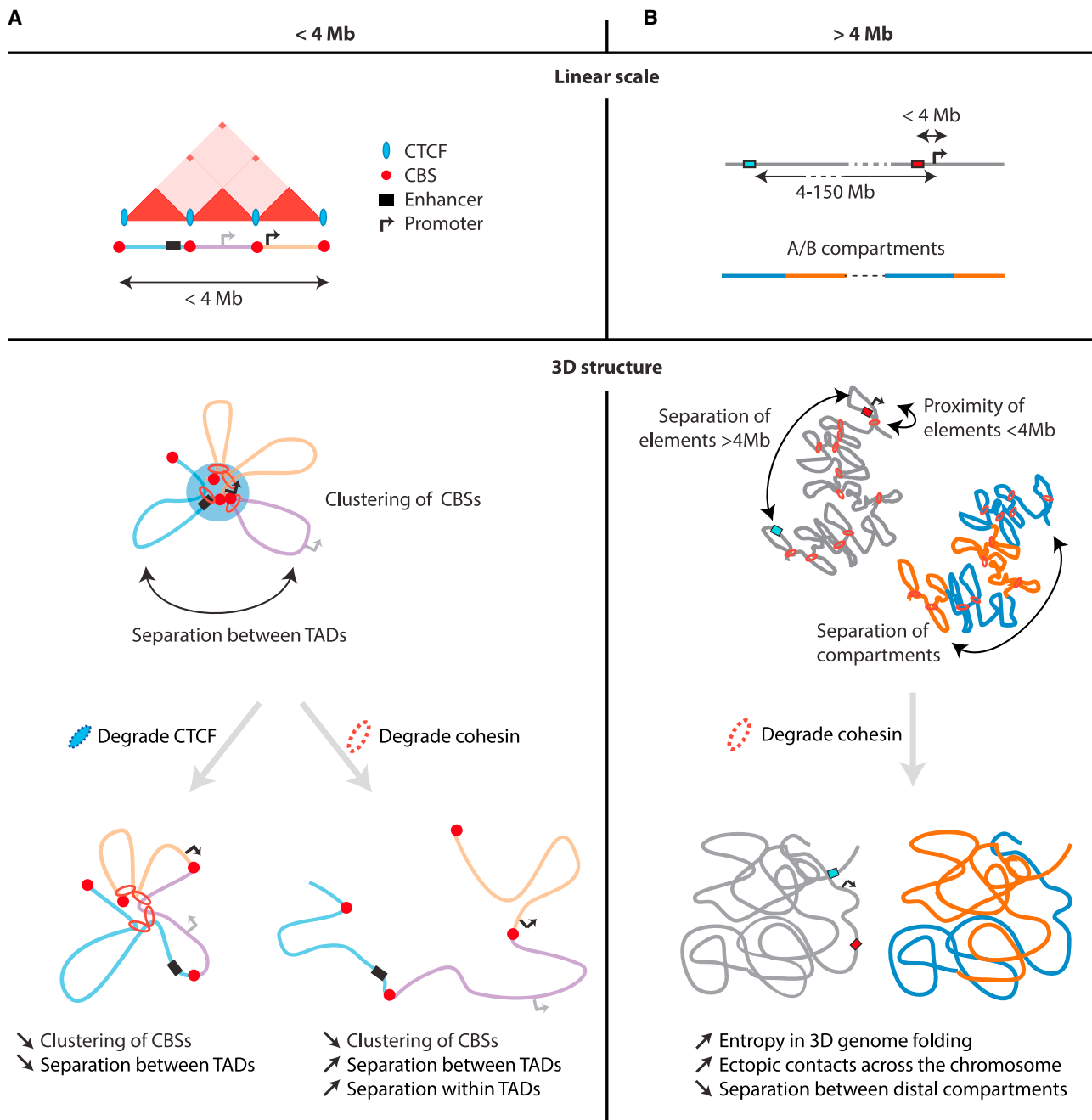


Figure 7. Loop stacking organizes the genome from TADs to chromosomes

(A) Schematic of contact frequency of a domain spanning three TADs and a 3D structure for the same sequence that we can derive from ORCA. Our data and modeling show rosette-like structures with CBSs clustering at the center of the structures and TADs spreading out radially. Degradation of CTCF or cohesin disrupts this organization. CTCF degradation leads to loss of CBS clustering but a similar overall number of loops. Cohesin degradation decreases the number of loops and leads to an overall expansion, both within and between TADs. The rosette organization has implications for gene regulation by enabling cross-TAD contact between enhancers and promoters that lie close to TAD boundaries.

(B) At the chromosome scale, loops enable a more linear organization of the genome by maintaining proximity between genetically proximal regions ($< 4 \text{ Mb}$) and keeping genetically distal regions ($> 4 \text{ Mb}$) apart. Degradation of cohesin leads to a disordered chromosome structure. This has implications for gene regulation, as enhancers and promoters normally at the opposite ends of the chromosome are in more frequent contact without cohesin. Loss of a linear chromosome structure also affects compartmentalization, by enabling increased contact between non-adjacent A-A or B-B domains.

shorter-range Pc loops were also reported to show less change or increase interaction by Hi-C,⁴ an effect readily explained by the loop-clash model that would not be expected if cohesin linear scanning were to knock apart Pc-Pc loops.

Thus, our work illustrates how chromatin loops and loop-loop interactions affect genome folding, from the sub-TAD scale to the whole chromosome, with implications for transcriptional regulation and epigenetic interactions.

Limitations of the study

Although we identify multi-loop stacks that are dependent on the presence of CTCF and cohesin, our inference that cohesin sits at the base of these loops is indirect, as we do not directly visualize cohesin or CTCF on the chromatin fiber. Our data do not distinguish whether the CTCF and cohesin molecules are in molecular contact—the genomic resolution of the traces and corresponding uncertainty in the nanoscale position precludes measuring protein-scale contacts, even while resolving the larger-scale loops of the chromatin fiber. Smaller scale loops along these paths, including those which may arise from short extrusion events, are also unresolved in our data. In exploring potential biophysical mechanisms that could give rise to loop stacking and its consequent effects on TADs, TAD bypass, and multi-scale genome organization, we focused on models involving cohesin-mediated loop extrusion. It is quite likely other biophysical models, such as the strings and binders switch model,^{68,69} can produce a similar agreement to our data without invoking active loop extrusion. We focus on loop extrusion due to the minimal number of parameters that must be inferred and increasing evidence *in vitro* and *in vivo* for its role in the genome architecture.^{8,20}

STAR★METHODS

Detailed methods are provided in the online version of this paper and include the following:

- KEY RESOURCES TABLE
- RESOURCE AVAILABILITY
 - Lead contact
 - Materials availability
 - Data and code availability
- EXPERIMENTAL MODEL AND SUBJECT DETAILS
 - Cell lines
- METHOD DETAILS
 - Cell culture, treatment, and collection
 - Western blot
 - Multiplexed cell labeling
 - Cell plating for imaging
 - ORCA primary probe hybridization
 - ORCA imaging
 - Immunofluorescence followed by ORCA
- QUANTIFICATION AND STATISTICAL ANALYSIS
 - Loop extrusion simulations
 - Image processing and quantification
 - ORCA analyses
 - Published genomic data

SUPPLEMENTAL INFORMATION

Supplemental information can be found online at <https://doi.org/10.1016/j.molcel.2023.04.008>.

ACKNOWLEDGMENTS

We thank Max Imakaev and Neil Chowdhury for code sharing and feedback on the polymer simulations; the 4DN community for support and the opportunities to present this work; Andrea Cosolo, Rahi Navelkar, and Andrew Schroeder (4DN) for help with formatting and uploading the data to the 4DN server; Allison Dear and Kevin Wang's lab at Stanford for assistance with western blots; Liang-Fu Chen, Tzuchiao Hung, and Carly Walker for comments on the manuscript; and current and former members of the Boettiger lab for feedback and discussion. This work was supported by NIH grants U01DK127419 and DP2GM132935A, the Packard Foundation, and a Beckman Young Investigators Award to A.N.B. A.H. was supported by Walter and Idun V. Berry Postdoctoral fellowship. M.P. was supported by a postdoctoral fellowship from the Damon Runyon Cancer Research Foundation. S.E.B. was supported by the Stanford Graduate fellowship. S.E.M. was supported by the Stanford Bio-X SIGF fellowship.

AUTHOR CONTRIBUTIONS

A.H. and A.N.B. designed the experiments. A.H., M.P., S.E.B., and S.E.M. performed the experiments. E.P.N. contributed key reagents. A.H. and A.N.B. performed analysis and interpreted the results. A.H. and A.N.B., wrote the manuscript with input from E.P.N., S.E.B., S.E.M., and M.P.

DECLARATION OF INTERESTS

The authors declare no competing interests.

INCLUSION AND DIVERSITY

We support inclusive, diverse, and equitable conduct of research.

Received: August 23, 2022

Revised: February 17, 2023

Accepted: April 6, 2023

Published: May 4, 2023

REFERENCES

1. Nora, E.P., Goloborodko, A., Valton, A.-L., Gibcus, J.H., Uebersohn, A., Abdennur, N., Dekker, J., Mirny, L.A., and Bruneau, B.G. (2017). Targeted degradation of CTCF decouples local insulation of chromosome domains from genomic compartmentalization. *Cell* **169**, 930–944.e22.
2. Rao, S.S.P., Huang, S.C., Glenn St Hilaire, B., Engreitz, J.M., Perez, E.M., Kieffer-Kwon, K.R., Sanborn, A.L., Johnstone, S.E., Bascom, G.D., Bochkov, I.D., et al. (2017). Cohesin loss eliminates all loop domains. *Cell* **171**, 305–320.e24.
3. Bintu, B., Mateo, L.J., Su, J.-H., Sinnott-Armstrong, N.A., Parker, M., Kinrot, S., Yamaya, K., Boettiger, A.N., and Zhuang, X. (2018). Super-resolution chromatin tracing reveals domains and cooperative interactions in single cells. *Science* **362**, eaau1783.
4. Rhodes, J.D.P., Feldmann, A., Hernández-Rodríguez, B., Díaz, N., Brown, J.M., Fursova, N.A., Blackledge, N.P., Prathapan, P., Dobrinic, P., Huseyin, M.K., et al. (2020). Cohesin disrupts Polycomb-dependent chromosome interactions in embryonic stem cells. *Cell Rep.* **30**, 820–835.e10.
5. Kubo, N., Ishii, H., Xiong, X., Bianco, S., Meitinger, F., Hu, R., Hocker, J.D., Conte, M., Gorkin, D., Yu, M., et al. (2021). Promoter-proximal CTCF binding promotes distal enhancer-dependent gene activation. *Nat. Struct. Mol. Biol.* **28**, 152–161. <https://doi.org/10.1038/s41594-020-00539-5>.

6. Fudenberg, G., Imakaev, M., Lu, C., Goloborodko, A., Abdennur, N., and Mirny, L.A. (2016). Formation of chromosomal domains by loop extrusion. *Cell Rep.* **15**, 2038–2049.
7. Sanborn, A.L., Rao, S.S.P., Huang, S.C., Durand, N.C., Huntley, M.H., Jewett, A.I., Bochkov, I.D., Chinnappan, D., Cutkosky, A., Li, J., et al. (2015). Chromatin extrusion explains key features of loop and domain formation in wild-type and engineered genomes. *Proc. Natl. Acad. Sci. USA* **112**, E6456–E6465.
8. Mirny, L., and Dekker, J. (2022). Mechanisms of chromosome folding and nuclear organization: their interplay and open questions. *Cold Spring Harb. Perspect. Biol.* **14**, a040147. <https://doi.org/10.1101/cshperspect.a040147>.
9. Luppino, J.M., Park, D.S., Nguyen, S.C., Lan, Y., Xu, Z., Yunker, R., and Joyce, E.F. (2020). Cohesin promotes stochastic domain intermingling to ensure proper regulation of boundary-proximal genes. *Nat. Genet.* **52**, 840–848.
10. Szabo, Q., Donjon, A., Jerković, I., Papadopoulos, G.L., Cheutin, T., Bonev, B., Nora, E.P., Bruneau, B.G., Bantignies, F., and Cavalli, G. (2020). Regulation of single-cell genome organization into TADs and chromatin nanodomains. *Nat. Genet.* **52**, 1151–1157.
11. Allahyar, A., Vermeulen, C., Bouwman, B.A.M., Krijger, P.H.L., Verstegen, M.J.A.M., Geelen, G., van Kranenburg, M., Pieterse, M., Straver, R., Haarhuis, J.H.I., et al. (2018). Enhancer hubs and loop collisions identified from single-allele topologies. *Nat. Genet.* **50**, 1151–1160.
12. Liu, M., Lu, Y., Yang, B., Chen, Y., Radda, J.S.D., Hu, M., Katz, S.G., and Wang, S. (2020). Multiplexed imaging of nucleome architectures in single cells of mammalian tissue. *Nat. Commun.* **11**, 2907.
13. Su, J.H., Zheng, P., Kinrot, S.S., Bintu, B., and Zhuang, X. (2020). Genome-scale imaging of the 3D organization and transcriptional activity of chromatin. *Cell* **182**, 1641–1659.e26.
14. Takei, Y., Yun, J., Zheng, S., Olikainen, N., Pierson, N., White, J., Shah, S., Thomassie, J., Suo, S., Eng, C.-H.L., et al. (2021). Integrated spatial genomics reveals global architecture of single nuclei. *Nature* **590**, 344–350.
15. Mateo, L.J., Murphy, S.E., Hafner, A., Cinquini, I.S., Walker, C.A., and Boettiger, A.N. (2019). Visualizing DNA folding and RNA in embryos at single-cell resolution. *Nature* **568**, 49–54.
16. Gehring, J., Hwee Park, J., Chen, S., Thomson, M., and Pachter, L. (2020). Highly multiplexed single-cell RNA-seq by DNA oligonucleotide tagging of cellular proteins. *Nat. Biotechnol.* **38**, 35–38.
17. Chen, L.-F., Long, H.K., Park, M., Swigut, T., Boettiger, A.N., and Wysocka, J. (2022). Structural elements facilitate extreme long-range gene regulation at a human disease locus. <https://doi.org/10.1101/2022.10.20.513057>.
18. Nuebler, J., Fudenberg, G., Imakaev, M., Abdennur, N., and Mirny, L.A. (2018). Chromatin organization by an interplay of loop extrusion and compartmental segregation. *Proc. Natl. Acad. Sci. USA* **115**, E6697–E6706.
19. Imakaev, M., Goloborodko, A., and Brandao, H. (2019). polychrom: polymer simulations of chromosomes and generating “in silico” Hi-C maps (GitHub). <https://zenodo.org/badge/latestdoi/178608195>.
20. Davidson, I.F., and Peters, J.-M. (2021). Genome folding through loop extrusion by SMC complexes. *Nat. Rev. Mol. Cell Biol.* **22**, 445–464.
21. Berlivet, S., Paquette, D., Dumouchel, A., Langlais, D., Dostie, J., and Kmita, M. (2013). Clustering of tissue-specific sub-tads accompanies the regulation of HoxA genes in developing limbs. *PLoS Genet.* **9**, e1004018.
22. Yun, H., Narayan, N., Vohra, S., Giopoulos, G., Mupo, A., Madrigal, P., Sasca, D., Lara-Astiaso, D., Horton, S.J., Agrawal-Singh, S., et al. (2021). Mutational synergy during leukemia induction remodels chromatin accessibility, histone modifications and three-dimensional DNA topology to alter gene expression. *Nat. Genet.* **53**, 1443–1455.
23. Wilderman, A., D'haene, E., Baetens, M., Yankee, T.N., Winchester, E.W., Glidden, N., Roets, E., Van Dorpe, J., Vergult, S., Cox, T.C., et al. (2022). A distant global control region is essential for normal expression of anterior HOXA genes during mouse and human craniofacial development. <https://doi.org/10.1101/2022.03.10.483852>.
24. Weber, C.M., Hafner, A., Kirkland, J.G., Braun, S.M.G., Stanton, B.Z., Boettiger, A.N., and Crabtree, G.R. (2021). mSWI/SNF promotes Polycomb repression both directly and through genome-wide redistribution. *Nat. Struct. Mol. Biol.* **28**, 501–511.
25. Murphy, S., and Boettiger, A.N. (2022). Polycomb repression of Hox genes involves spatial feedback but not domain compaction or demixing. <https://doi.org/10.1101/2022.10.14.512199>.
26. Polovnikov, K., Belan, S., Imakaev, M., Brandão, H.B., and Mirny, L.A. (2022). Fractal polymer with loops recapitulates key features of chromosome organization. <https://doi.org/10.1101/2022.02.01.478588>.
27. Schwarzer, W., Abdennur, N., Goloborodko, A., Pekowska, A., Fudenberg, G., Loe-Mie, Y., Fonseca, N.A., Huber, W., Haering, C.H., Mirny, L.A., et al. (2017). Two independent modes of chromatin organization revealed by cohesin removal. *Nature* **551**, 51–56.
28. Lieberman-Aiden, E., van Berkum, N.L., Williams, L., Imakaev, M., Ragoczy, T., Telling, A., Amit, I., Lajoie, B.R., Sabo, P.J., Dorschner, M.O., et al. (2009). Comprehensive mapping of long-range interactions reveals folding principles of the human genome. *Science* **326**, 289–293.
29. Ou, H.D., Phan, S., Deerinck, T.J., Thor, A., Ellisman, M.H., and O'Shea, C.C. (2017). ChromEMT: visualizing 3D chromatin structure and compaction in interphase and mitotic cells. *Science* **357**, eaag0025. <https://doi.org/10.1126/science.aag0025>.
30. Finn, E.H., Pegoraro, G., Brandão, H.B., Valton, A.-L., Oomen, M.E., Dekker, J., Mirny, L., and Misteli, T. (2019). Extensive heterogeneity and intrinsic variation in spatial genome organization. *Cell* **176**, 1502–1515.e10.
31. Wang, S., Su, J.-H., Beliveau, B.J., Bintu, B., Moffitt, J.R., Wu, C.-T., and Zhuang, X. (2016). Spatial organization of chromatin domains and compartments in single chromosomes. *Science* **353**, 598–602.
32. Hsieh, T.-H.S., Cattoglio, C., Slobodyanyuk, E., Hansen, A.S., Darzacq, X., and Tjian, R. Enhancer-promoter interactions and transcription are maintained upon acute loss of CTCF, cohesin, WAPL, and YY1. Preprint at bioRxiv, 10.1101/2021.07.14.452365.
33. Aljahani, A., Hua, P., Karpinska, M.A., Quililan, K., Davies, J.O.J., and Oudelaar, A.M. (2022). Analysis of sub-kilobase chromatin topology reveals nano-scale regulatory interactions with variable dependence on cohesin and CTCF. *Nat. Commun.* **13**, 2139.
34. Liu, N.Q., Maresca, M., van den Brand, T., Braccioli, L., Schijns, M.M.G.A., Teunissen, H., Bruneau, B.G., Nora, E.P., and de Wit, E. (2021). WAPL maintains a cohesin loading cycle to preserve cell-type-specific distal gene regulation. *Nat. Genet.* **53**, 100–109.
35. Bates, L.E., Alves, M.R.P., and Silva, J.C.R. (2021). Auxin-degron system identifies immediate mechanisms of OCT4. *Stem Cell Rep.* **16**, 1818–1831.
36. Jaeger, M.G., Schwalb, B., Mackowiak, S.D., Velychko, T., Hanzl, A., Imrichova, H., Brand, M., Agerer, B., Chorn, S., Nabet, B., et al. (2020). Selective Mediator dependence of cell-type-specifying transcription. *Nat. Genet.* **52**, 719–727.
37. Muhar, M., Ebert, A., Neumann, T., Umkehrer, C., Jude, J., Wieshofer, C., Rescheneder, P., Lipp, J.J., Herzog, V.A., Reichholf, B., et al. (2018). SLAM-seq defines direct gene-regulatory functions of the BRD4-MYC axis. *Science* **360**, 800–805.
38. Lupiáñez, D.G., Kraft, K., Heinrich, V., Krawitz, P., Brancati, F., Klopocki, E., Horn, D., Kayserili, H., Opitz, J.M., Laxova, R., et al. (2015). Disruptions of topological chromatin domains cause pathogenic rewiring of gene-enhancer interactions. *Cell* **161**, 1012–1025.
39. Flavahan, W.A., Drier, Y., Liau, B.B., Gillespie, S.M., Venteicher, A.S., Stemmer-Rachamimov, A.O., Suvà, M.L., and Bernstein, B.E. (2015). Insulator dysfunction and oncogene activation in IDH mutant gliomas. *Nature* **529**, 110–114.
40. Hnisz, D., Weintraub, A.S., Day, D.S., Valton, A.-L., Bak, R.O., Li, C.H., Goldmann, J., Lajoie, B.R., Fan, Z.P., Sigova, A.A., et al. (2016).

- Activation of proto-oncogenes by disruption of chromosome neighborhoods. *Science* 351, 1454–1458.
41. Hnisz, D., Day, D.S., and Young, R.A. (2016). Insulated neighborhoods: structural and functional units of mammalian gene control. *Cell* 167, 1188–1200.
 42. Gerasimova, T.I., Byrd, K., and Corces, V.G. (2000). A chromatin insulator determines the nuclear localization of DNA. *Mol. Cell* 6, 1025–1035.
 43. Gombert Wendy, M., Farris Stephen, D., Rubio Eric, D., Morey-Rosler, K.M., Schubach William, H., and Krumm, A. (2003). The c-myc Insulator Element and Matrix attachment Regions Define the c-myc Chromosomal Domain. *Mol. Cell. Biol.* 23, 9338–9348.
 44. Montavon, T., Soshnikova, N., Mascrez, B., Joye, E., Thevenet, L., Splinter, E., de Laat, W., Spitz, F., and Duboule, D. (2011). A regulatory archipelago controls hox genes transcription in digits. *Cell* 147, 1132–1145.
 45. Guo, Y., Monahan, K., Wu, H., Gertz, J., Varley, K.E., Li, W., Myers, R.M., Maniatis, T., and Wu, Q. (2012). CTCF/cohesin-mediated DNA looping is required for protocadherin α promoter choice. *Proc. Natl. Acad. Sci. USA* 109, 21081–21086.
 46. Shih, H.-Y., Verma-Gaur, J., Torkamani, A., Feeney, A.J., Galjart, N., and Krangel, M.S. (2012). *Tcra* gene recombination is supported by a *Tcra* enhancer- and CTCF-dependent chromatin hub. *Proc. Natl. Acad. Sci. USA* 109, E3493–E3502.
 47. Labrador, M., and Corces, V.G. (2002). Setting the boundaries of chromatin domains and nuclear organization. *Cell* 111, 151–154.
 48. Phillips, J.E., and Corces, V.G. (2009). CTCF: master weaver of the genome. *Cell* 137, 1194–1211.
 49. Gómez-Díaz, E., and Corces, V.G. (2014). Architectural proteins: regulators of 3D genome organization in cell fate. *Trends Cell Biol.* 24, 703–711.
 50. Kyrchanova, O., and Georgiev, P. (2014). Chromatin insulators and long-distance interactions in Drosophila. *FEBS Lett.* 588, 8–14.
 51. Oudehaar, A.M., Davies, J.O.J., Hanssen, L.L.P., Telenius, J.M., Schwessinger, R., Liu, Y., Brown, J.M., Downes, D.J., Chiariello, A.M., Bianco, S., et al. (2018). Single-allele chromatin interactions identify regulatory hubs in dynamic compartmentalized domains. *Nat. Genet.* 50, 1744–1751.
 52. Wang, X.Q.D., Gore, H., Himadewi, P., Feng, F., Yang, L., Zhou, W., Liu, Y., Wang, X., Chen, C.-W., Su, J., et al. (2020). Three-dimensional regulation of HOXA cluster genes by a cis-element in hematopoietic stem cell and leukemia. <https://doi.org/10.1101/2020.04.16.2017533>.
 53. Hung, T.-C., Kingsley, D.M., and Boettiger, A. (2023). Boundary stacking interactions enable cross-TAD enhancer-promoter communication during limb development. <https://doi.org/10.1101/2023.02.06.527380>.
 54. Huang, H., Zhu, Q., Jussila, A., Han, Y., Bintu, B., Kern, C., Conte, M., Zhang, Y., Bianco, S., Chiariello, A.M., et al. (2021). CTCF mediates dosage- and sequence-context-dependent transcriptional insulation by forming local chromatin domains. *Nat. Genet.* 53, 1064–1074.
 55. Chakraborty, S., Kopitchinski, N., Zuo, Z., Eraso, A., Awasthi, P., Chari, R., Mitra, A., Tobias, I.C., Moorthy, S.D., Dale, R.K., et al. (2023). Enhancer-promoter interactions can bypass CTCF-mediated boundaries and contribute to phenotypic robustness. *Nat. Genet.* 55, 280–290. <https://doi.org/10.1038/s41588-022-01295-6>.
 56. Wang, W., Ren, G., Hong, N., and Jin, W. (2019). Exploring the changing landscape of cell-to-cell variation after CTCF knockdown via single cell RNA-seq. *BMC Genomics* 20, 1015.
 57. Ren, G., Jin, W., Cui, K., Rodriguez, J., Hu, G., Zhang, Z., Larson, D.R., and Zhao, K. (2017). CTCF-mediated enhancer-promoter interaction is a critical regulator of cell-to-cell variation of gene expression. *Mol. Cell* 67, 1049–1058.e6.
 58. Chiang, M., Brackley, C.A., Naughton, C., Nozawa, R.-S., Battaglia, C., Marenduzzo, D., and Gilbert, N. (2022). Gene structure heterogeneity drives transcription noise within human chromosomes. <https://doi.org/10.1101/2022.06.09.495447>.
 59. Cuartero, S., Weiss, F.D., Dharmalingam, G., Guo, Y., Ing-Simmons, E., Masella, S., Robles-Rebollo, I., Xiao, X., Wang, Y.F., Barozzi, I., et al. (2018). Control of inducible gene expression links cohesin to hematopoietic progenitor self-renewal and differentiation. *Nat. Immunol.* 19, 932–941.
 60. Pauli, A., Althoff, F., Oliveira, R.A., Heidmann, S., Schulziner, O., Lehner, C.F., Dickson, B.J., and Nasmyth, K. (2008). Cell-type-specific TEV Protease Cleavage reveals cohesin functions in Drosophila neurons. *Dev. Cell* 14, 239–251.
 61. Pauli, A., van Bemmel, J.G., Oliveira, R.A., Itoh, T., Shirahige, K., van Steensel, B., and Nasmyth, K. (2010). A direct role for cohesin in gene regulation and ecdysone response in Drosophila salivary glands. *Curr. Biol.* 20, 1787–1798.
 62. Cummings, C.T., and Rowley, M.J. (2022). Implications of dosage deficiencies in CTCF and cohesin on genome organization, gene expression, and human neurodevelopment. *Genes* 13, 583. <https://doi.org/10.3390/genes13040583>.
 63. Avagliano, L., Parenti, I., Grazioli, P., Di Fede, E., Parodi, C., Mariani, M., Kaiser, F.J., Selicorni, A., Gervasini, C., and Massa, V. (2020). Chromatinopathies: A focus on Cornelia de Lange syndrome. *Clin. Genet.* 97, 3–11.
 64. Di Nardo, M., Pallotta, M.M., and Musio, A. (2022). The multifaceted roles of cohesin in cancer. *J. Exp. Clin. Cancer Res.* 41, 96.
 65. Bantignies, F., Roure, V., Comet, I., Leblanc, B., Schuettengruber, B., Bonnet, J., Tixier, V., Mas, A., and Cavalli, G. (2011). Polycomb-dependent regulatory contacts between distant hox loci in Drosophila. *Cell* 144, 214–226.
 66. Oksuz, O., Narendra, V., Lee, C.H., Descostes, N., LeRoy, G., Raviram, R., Blumenberg, L., Karch, K., Rocha, P.P., Garcia, B.A., et al. (2018). Capturing the onset of PRC2-mediated repressive domain formation. *Mol. Cell* 70, 1149–1162.e5.
 67. Kraft, K., Yost, K.E., Murphy, S.E., Magg, A., Long, Y., Corces, M.R., Granja, J.M., Wittler, L., Mundlos, S., Cech, T.R., et al. (2022). Polycomb-mediated genome architecture enables long-range spreading of H3K27 methylation. *Proc. Natl. Acad. Sci. USA* 119, e2201883119.
 68. Conte, M., Fiorillo, L., Bianco, S., Chiariello, A.M., Esposito, A., and Nicodemi, M. (2020). Polymer physics indicates chromatin folding variability across single-cells results from state degeneracy in phase separation. *Nat. Commun.* 11, 3289.
 69. Barbieri, M., Chotalia, M., Fraser, J., Lavitas, L.-M., Dostie, J., Pombo, A., and Nicodemi, M. (2012). Complexity of chromatin folding is captured by the strings and binders switch model. *Proc. Natl. Acad. Sci. USA* 109, 16173–16178.
 70. Bonev, B., Mendelson Cohen, N., Szabo, Q., Fritsch, L., Papadopoulos, G.L., Lubling, Y., Xu, X., Lv, X., Hugnot, J.-P., Tanay, A., et al. (2017). Multiscale 3D genome rewiring during mouse neural development. *Cell* 171, 557–572.e24.
 71. Arruda, N.L., Carico, Z.M., Justice, M., Liu, Y.F., Zhou, J., Stefan, H.C., and Dowen, J.M. (2020). Distinct and overlapping roles of STAG1 and STAG2 in cohesin localization and gene expression in embryonic stem cells. *Epigenetics Chromatin* 13, 32.
 72. Hooper, M., Hardy, K., Handyside, A., Hunter, S., and Monk, M. (1987). HPRT-deficient (Lesch-Nyhan) mouse embryos derived from germline colonization by cultured cells. *Nature* 326, 292–295.
 73. Mateo, L.J., Sinnott-Armstrong, N., and Boettiger, A.N. (2021). Tracing DNA paths and RNA profiles in cultured cells and tissues with ORCA. *Nat. Protoc.* 16, 1647–1713.
 74. Stringer, C., Wang, T., Michaelos, M., and Pachitariu, M. (2021). Cellpose: a generalist algorithm for cellular segmentation. *Nat. Methods* 18, 100–106.
 75. Abdennur, N., and Mirny, L.A. (2020). Cooler: scalable storage for Hi-C data and other genetically labeled arrays. *Bioinformatics* 36, 311–316.
 76. Rigano, A., Ehmsen, S., Öztürk, S.U., Ryan, J., Balashov, A., Hammer, M., Kirli, K., Boehm, U., Brown, C.M., Bellve, K., et al. (2021). Micro-Meta

- App: an interactive tool for collecting microscopy metadata based on community specifications. *Nat. Methods* 18, 1489–1495.
77. Eastman, P., Swails, J., Chodera, J.D., McGibbon, R.T., Zhao, Y., Beauchamp, K.A., Wang, L.-P., Simmonett, A.C., Harrigan, M.P., Stern, C.D., et al. (2017). OpenMM 7: Rapid development of high performance algorithms for molecular dynamics. *PLoS Comput. Biol.* 13, e1005659.
78. (2017). A conversation with Leonid Mirny. *Cold Spring Harb. Symp. Quant. Biol.* 82, 403–405.
79. Igoshin, O.A., Chen, J., Xing, J., Liu, J., Elston, T.C., Grabe, M., Kim, K.S., Nirody, J.A., Rangamani, P., Sun, S.X., et al. (2019). Biophysics at the coffee shop: lessons learned working with George Oster. *Mol. Biol. Cell* 30, 1882–1889.

STAR★METHODS

KEY RESOURCES TABLE

REAGENT or RESOURCE	SOURCE	IDENTIFIER	
Antibodies			
Anti-Geminin antibody	Abcam	ab195047	
Anti-RAD21 antibody	Abcam	ab154769	
Anti-CTCF antibody	Abcam	ab128873	
Anti-Actin antibody	Cell Signaling	3700	
Anti-HA antibody	Abcam	ab9110	
Anti-V5 antibody	Abcam	ab27671	
Chemicals, peptides, and recombinant proteins			
Indole – 3 – acetic acid sodium salt (auxin analog)	Sigma-Aldrich	i2886	
dTAG-13	Fisher	Tocris 6605/5	
TCO-PEG4-TFP Ester	Click Chemistry Tools	1398-2	
Methyltetrazine-PEG4-Amine	Click Chemistry Tools	1012-100	
Methyltetrazine-NHS Ester	Click Chemistry Tools	1128-25	
Deposited data			
ORCA processed data	This study	4DN data portal: https://data.4dnucleome.org/A_Hafner_mESC_loop_stacking_chromatin_tracing https://doi.org/10.17632/gfk7nvgkcp.1	
Unprocessed Western blot images	This study		
Hi-C (mESs control and RAD21 degraded cells)	Rhodes et al. ⁴	E-MTAB-7816	
Hi-C (mESs control and CTCF degraded cells)	Nora et al. ¹	GSE98671	
CTCF ChIP-seq in mESCs	Bonev et al. ⁷⁰	GSE96107	
RAD21 ChIP-seq in mESCs	Arruda et al. ⁷¹	GSE144116	
Ring1B ChIP-seq in mESCs	Bonev et al. ⁷⁰	GSE96107	
Experimental models: Cell lines			
E14TG2a (referred to as E14)	Hooper et al. ⁷²	N/A	
E14TG2a CTCF-AID (clone)	Nora et al. ¹	N/A	
E14TG2a RAD21-AID (clone)	Szabo et al. ¹⁰		
EED-dTAG and Ring1B-dTAG mES cells	Weber et al. ²⁴		
Oligonucleotides			
ORCA oligos	Table S2	N/A	
Cell barcode oligos (subset of ORCA barcodes with 3prime amine modification)	Table S2	N/A	
Software and algorithms			
ORCA spot calling analysis	Mateo et al. ¹⁵ and Mateo et al. ⁷³	https://doi.org/10.5281/zenodo.7698979	
Open2C polymer simulations	Imakaev et al. ¹⁹ and This work	https://doi.org/10.5281/zenodo.7698987& https://doi.org/10.5281/zenodo.7761973	
CellPose cell segmentation	Stringer et al. ⁷⁴	N/A	
Cooler	Abdennur and Mirny ⁷⁵	N/A	

RESOURCE AVAILABILITY

Lead contact

Further information and requests for resources and reagents should be directed to and will be fulfilled by the lead contact, Alistair Boettiger (boettiger@stanford.edu).

Materials availability

This study did not generate new unique reagents.

Data and code availability

- All processed ORCA data and unprocessed Western blot images generated in this study have been deposited and are publicly available as of the date of publication. Accession numbers and DOI are listed in the [key resources table](#). The probe locations ([Table S1](#)) can also be viewed through the UCSC genome browser: https://genome.ucsc.edu/s/tonia/mm10_Hafner2023
- All original code has been deposited at Github and Zenodo and is publicly available as of the date of publication. DOIs are listed in the [key resources table](#).
- Any additional information required to reanalyze the data reported in this paper is available from the [lead contact](#) upon request.

EXPERIMENTAL MODEL AND SUBJECT DETAILS**Cell lines**

E14 mouse embryonic stem cells (E14Tg2a 129/Ola) and the derived Rad21-AID (clone EN272.2) and CTCF-AID (clone EN52.9.1) cell lines were a gift from Elphege Nora. Ring1B and EED dTAG cell line (derived from TC1(129) mouse ESCs) was a gift from Christopher Weber and the Crabtree lab.

METHOD DETAILS**Cell culture, treatment, and collection**

Cells were cultured in Knockout Dulbecco's modified Eagles medium (Thermo Fisher, cat. No. 10829-018), 15% qualified embryonic stem cell FBS (Thermo Fisher, cat. No. 16141079), 1x GlutaMAX™ Supplement (Thermo Fisher, cat. No. 16141079), 1x Gibco™ Penicillin-Streptomycin (Thermo Fisher cat. No. 15140122), 1x MEM Non-Essential Amino Acids Solution (Thermo Fisher cat. No. 11140050), 10mM HEPES (Thermo Fisher cat. No. 15630080), 0.1mM β-mercaptoethanol (Thermo Fisher cat. No. 21985023) and LIF (final 1000 U/ml, Millipore Sigma ESG1107). E14, CTCF-AID and RAD21-AID mESCs were grown on 0.1% gelatin. Ring1B and EED dTAG mESCs cells were grown on 0.1% gelatin coated dishes with EmbryoMax® Primary Mouse Embryonic Fibroblasts (Sigma, PMEF-CF).

To degrade CTCF or RAD21, a final concentration of 500μM IAA (Sigma i2886) was used for all experiments. Cells were treated for 4 hours, media was changed in the untreated condition at the same time as the fresh media with auxin was added to auxin treated cells. To degrade EED and RING1b, dTAG-13 was added for 8 h at 500 nM as previously described.^{24,25}

For cell collection, cells were trypsinized, counted, spun down and after removal of supernatant media, were fixed in suspension in 4%PFA in 1xPBS on a nutator for 10 minutes, washed 3 times with 1xPBS, resuspended in 70%EtOH in 1xPBS at a concentration of 1-10 000 cells/ul and stored at -20C for up to 6 months. For Ring1B and EED dTAG mESCs grown on feeder cells, serial replating was performed on 0.1% gelatin coated plates in order to deplete the feeder cells prior to collection.

Western blot

Cells were collected by trypsinization, washed in 1xPBS and pellets were frozen on dry ice/EtOH bath and stored at -80C. Cells were lysed in mRIPA buffer with Protease and Phosphatase inhibitor cocktail. 20ug of protein was run on a 4-20% Mini-PORTEAN TGX precast gels in Tris-Glycine-SDS running buffer. After transfer onto the nitrocellulose membrane, and blocking in Li-Cor Intercept Blocking Buffer (TBS), blots were probed with either CTCF (Abcam 128873, 1:1000) or Rad21 (Abcam 154769, 1:1000) antibodies as well as beta-Actin (Cell Signaling 3700) in blocking buffer at 4C overnight. Membranes were then washed 3x 5min in TBST at room temperature, incubated with secondary antibodies (Li-Cor: IRDye 680RD Donkey anti-Rabbit 926-68073 and IRDye 800CW Donkey anti-Mouse, 1:10 000 diluted in blocking buffer) for 1h at room temperature. After 3x 5 min washes in TBST, and 1 wash in TBS, samples were imaged on the Li-Cor scanner.

Western blot for Ring1b and EED ([Figure S3E](#)) was reproduced from Murphy and Boettiger.²⁵ The protocol is the same as above but with the following antibodies: V5 tag (abcam 27671, 1:800), targeting the V5-tagged EED; HA-tag (abcam 9110) (labeling the HA-tagged RING1b, 1:800).

Multiplexed cell labeling

The multiplexed cell labeling protocol was adapted from Gehring et al.¹⁶ The detailed protocol is as follows.

Part 1.: Preparation of labelled oligos

- 1) 3' amine-modified oligos were ordered from IDT ([Table S2](#)) and resuspended to 500 μM in 50 mM sodium borate buffer pH 8.5.
- 2) In 1.5 mL microcentrifuge tube, 25.0 μL 3' amine-modified oligo was added into 50 mM sodium borate buffer, 8.2 μL 10 mM Methyltetrazine-NHS ester, 41.8 μL DMSO, and incubated, protected from light, for 30 minutes with agitation.
- 3) After 30 minutes, another 8.2 μL 10 mM Methyltetrazine-NHS ester was added and then added once again after an additional 30 minutes.

- 4) The reaction was quenched by adding 180 μ L 50 mM sodium borate buffer and 30 μ L 3 M NaCl, followed by addition of 750 μ L ice cold 100% EtOH.
- 5) We then precipitated @ -80 °C overnight.
- 6) Contents were transferred to ultracentrifuge tubes and spun at 20,000xg for 30 minutes at 4°C.
- 7) Pellets were then washed twice with 750 μ L 70% EtOH, ensuring not to disrupt the pellet (don't mix pipette) and let to dry for ~10 minutes in fume hood until nearly all ethanol was evaporated.
- 8) Pellets were resuspended in 100 μ L cold HEPES buffer.
- 9) Typical concentration is around ~80 μ M.

Part 2.: Cell labeling

- 1) Between 500K and 5M fixed cells (stored in 70%EtOH in 1xPBS at -20C) were washed twice in 1xPBS and resuspended in 100ul of 1xPBS.
- 2) 4 μ L of 1 mM TCO-PEG4-TFP Ester was added to the cells, mixed by pipetting and incubated for 5 min @RT protected from light.
- 3) 6 μ L of each methyltetrazine oligo amide (prepared in Part 1) was added, mixed by pipetting and incubated for 30 min @RT protected from light.
- 4) Methyltetrazine-PEG4-Amine was added for final concentration of 50 μ M and Tris HCl was added to 10 mM final concentration and incubated for 5 min @RT.
- 5) Cells were then diluted ~twofold with 1X PBS, spun down and washed 3x in 1xPBS.
- 6) Cells were resuspended in 70% EtOH in 1xPBS, and kept -20C for up to 6 months after the initial cell collection date.

Cell plating for imaging

Cells stored in suspension at -20°C were resuspended by pipetting. Barcoded cells were combined at desired ratios in a single tube. A small volume of cells (~5ul of cells at 10k/ul-20k/ul concentration) was spotted on a poly-lysine coated area in the center of the slide and let dry for 3-5 min. 1xPBS was then added and the slide was inspected to check for optimal cell density (ideally monolayer of cells evenly covering the entire slide). Cells were then used for IF or ORCA. For the experiment with Ring1B and EED depletion, we did not barcode cells, but plated the two conditions (with or without dTAG) in two spatially distinct spots on the slide.

ORCA primary probe hybridization

For ORCA DNA experiments, we used the protocol described in Mateo et al.¹⁵ and in detail in Mateo et al. (2020). After cell plating, cells were permeabilized with 0.5% Triton-X in 1xPBS for 10 min, followed by 2 washes with 1x PBS. Cells were incubated in 0.1M HCl for 5 min followed by 3 washes in 1xPBS. We then treated cells for 30 min with RNase A (10 ug/ml) at 37°C followed by 3 washes in 2xSSC. Cells were then incubated for 35 min in Hybridization buffer (2xSSC, 50% formamide and 0.1% Tween). Primary probes (for ~2.5 Mb chr6 and chr3 probes, we used 15 ug of probe, for ~ 30 Mb and ~150 Mb scale tiling we used 3–4 ug of probe) diluted in hybridization solution (2xSSC, 50% formamide, 10% dextran sulfate, 0.1% Tween) were then added onto cells, covered with a cover-glass, denatured for 3min at 90C and incubated overnight at 42C. The following day, cells were washed with 2xSSC, postfixed in 2% GA, 8% PFA in 1xPBS for 30 min to 1 h and set up on the microscope for sequential labeling and imaging. If ORCA was preceded by IF, we picked positions to match as closely as possible to cells imaged by IF. Cell barcodes were either imaged before or after the ORCA probe barcodes.

RNA labeling was done as described above for DNA with the exception of the HCl, RNase A or post fix steps.

ORCA imaging

Samples hybridized with primary probes were imaged on the custom microscopy and microfluidics setup as previously described.^{15,73} The details of the microscope setups are also documented on the Micro-Meta App.⁷⁶ We used secondary oligos carrying either a Cy5 or a 750 dye complementary to the readout barcodes on primary probes. We used strand displacement to remove imaged barcodes prior to imaging the next barcode.

As fiducial we designed a subset of probes, either directly adjacent to the readout probes for the ~2.5Mb domains, or in the middle of the domain for the ~30 Mb and ~150 Mb domains, that carried a fiducial sequence, that we labeled with a secondary Cy3 oligo. These Cy3 fiducial probes were labeled at the first round of imaging, together with the first readout and were imaged at each subsequent round of imaging. The fiducial spots were subsequently used for registration and drift correction in the image analysis pipeline. We note that due to weak fiducial labeling for the ~2.5 Mb domains, we designed an adapter to bind to all probes for these domains.

Adapter sequences:

chr6_3Mb_fid_adapter: ATCGACCCGGCATAACGCCAATCGACGTGGGACATCAGC

chr3_3Mb_fid_adapter: ATCGACCCGGCATAACGCCACCCGCGTCGAGCCAGTTAG

Immunofluorescence followed by ORCA

Plated cells were permeabilized and blocked in antibody dilution buffer (2%BSA, 0.1% Triton X -100 in 1xPBS) for 10 min @RT. Cells were then incubated with the Geminin primary antibody (ab195047, 1:100) diluted in antibody dilution buffer for 1 h @ RT, washed 3x with 1xPBS, incubated with secondary antibody (anti-rabbit 647 Invitrogen A31573) and DAPI diluted in antibody dilution buffer for 30 min @RT, washed 3x with 1xPBS after which they were ready to image.

QUANTIFICATION AND STATISTICAL ANALYSIS

Loop extrusion simulations

Loop extrusion simulations were performed using the “polychrom” package from “open2c” github project,¹⁹ which was developed from earlier polymer models of loop extrusion written by the Mirny lab,^{6,18} and powered by the GPU accelerated molecular simulation toolkit openMM.⁷⁷ All simulations were run on an NVIDIA Titan Xp card. Polychrom uses a Langevin approach to simulate the dynamics of a polymer under several user defined energy constraints. Complete details of the energetic constraints and other parameters are specified in the python simulation scripts included in our github repository for this project: <https://github.com/BoettigerLab/Hafner2022/> and <https://github.com/BoettigerLab/polychrom>, and described in brief below. These can be run independently using polychrom, which may be downloaded from the polychrom github page: <https://github.com/open2c/polychrom>.

We simulated the chromosomes as 6 polymers confined in a spherical geometry representing the nucleus. Each polymer was 5,000 monomers long, corresponding to 30 kb/monomer (with monomer diameter ~50 nm) for 150 Mb chromosomes, on par with the probe size used at our 3 Mb, 30 Mb, and whole-chromosome (150 Mb) experiments. Each simulation was run in 600 independent replicates, for sufficient time that the final 3D structures were uncorrelated with the starting structure at all length scales and that the pattern of TADs and loops could be reproduced from averaging single replicates over time identically as to averaging over replicates (see below for loop extrusion and TADs).

Loop extrusion was simulated using the previously described sequential 1D and 3D simulations, implemented by *polychrom*. Briefly, the 1D simulations simulate the loading, unloading, and motion of loop extruders with left and right arms that walk bi-directionally on chromatin and interactions with extrusion blockers. These are followed by 3D simulations, in which short harmonic bonds between the left and right arms of the extrusion factors impose the loop. Loop extrusion blocking sites, simulating CTCF, were positioned along the 3Mb fiber as follows (in kb): [150, 870, 900, 1170, 1380, 1770, 2250, 2400, 2700], with the following probabilities for stalling extrusion factors: [.5,.95,.95,1,.4,.4,.95,.95,.5], acting in the following respective directions, where 0 is a bidirectional bloc, 1 a blocks extruders only from the right and 2 only from the left: [1 2 1 0 0 0 2 1 0]. This produced the contact pattern shown in Figure 1F. This 3 Mb pattern was replicated back to back to produce the 150 Mb chromosome pattern. 250 loop extruders (cohesin) loaded randomly with uniform probability across the chromatin fiber, and walked along chromatin with a half-life corresponding to 300 kb extrusion. The confinement radius for the nucleus was chosen so 20% of the nuclear volume was filled with polymer. Confinement volumes 0.02% were used to represent the unconstrained conditioned and 0.2 the 10% of relaxation volume condition. A hard-sphere repulsion energy of 3 was used in the low density and high density simulations, and later increased to 6 in “loop clash” simulations, which simulated a substantially reduced frequency of chain crossing. To simulate A/B compartmentalization, we divided each chromosome into 6 evenly sized blocks, alternating types A and B. Both A and B types were given weak homophilic interaction energies of 0.2, which resulted in mild demixing at the single trace level. See code available on github link above for details.

It should be emphasized that these are coarse-grained simulations, intended to capture the qualitative, emergent properties of a small number of physical processes – such as loop extruders moving on a large polymer in a confined volume. The utility of these coarse grained physics models is not to capture as many features of reality as possible in a common model, but rather to reproduce key patterns in the experimental data from a minimal mechanistic hypothesis.^{78,79} By using as few features from reality as possible in the model rather than as many as possible, we can develop deeper intuition about the underlying processes. As a consequence of coarse-graining abstraction, the precise relation between simulation units, monomers to kb, cohesin spacing to kb, monomer radii to nanometers, etc, are approximate. We did not undertake a comprehensive sweep of the parameter space of the model. The intensive computational time for the thousands of independent simulations limit such analysis, and showing that the multiscale qualitative effects of cohesin chromatin folding can be captured by loop extrusion did not require it.

Image processing and quantification

Image processing and spot calling for ORCA data

Image processing (drift correction and localization of spots) analysis was performed as described in Mateo et al.^{15,73} using ORCA analysis tools: <https://github.com/BoettigerLab/ORCA-public>.

Cell segmentation

We used the CellPose⁷⁴ for segmenting individual nuclei.

Geminin IF and cell size quantification

For Geminin IF quantification and the quantification of nuclear size, we performed all calculations on the experiments for the Hoxa and Sox2 domains for 2.2 and 2.8 Mb respectively where cells were stained for Dapi and Geminin prior to the ORCA experiments. Nuclear segmentation was done on Dapi staining using CellPose. The resulting cell masks were then used to quantify levels of Geminin immunofluorescence by computing the mean intensity per nucleus. The Geminin low population was defined as the lowest 25% of the

geminin expression level across all stained cells within the experiment (combined the E14 parental cell line together with CTCF-AID and Rad21-AID auxin treated and untreated cells).

Demultiplexing cell barcodes

For each fiducial spot, we quantified the intensity of each cell barcode signal. To normalize for differences in brightness across cell barcodes, we then balanced the intensities across all values. We used the nearest neighbors approach to classify each spot into groups based on the values for all cell barcodes for that spot.

RNA FISH data analysis

RNA FISH data was quantified similarly to Mateo et al.¹⁵ Briefly, images were maximum-z-projected and flatfield corrected. Foci corresponding to single mRNAs were identified by using a local-maxima search with manually defined thresholds. Foci positions were then overlaid with cell segmentation masks from CellPose to compute single-cell transcript mRNA counts.

ORCA analyses

Merge and filtering of ORCA data

For the ~2.5 Mb scale data, we had 2 technical replicates (performed on the same batch of collected and barcoded cells) and a biological replicate (independently thawed, treated, fixed and barcoded cells). Replicates showed a high degree of reproducibility and showed identical patterns of TADs and loops and were comparable in median distance (Figure S1C). We thus merged the data for all subsequent analyses. Barcodes with low hybridization efficiency (< 10 %) were filtered on the merged data. An additional filter was done on a dataset basis to remove obvious artifacts such as failed strand displacement events.

Determining the loop threshold

As described in text, to avoid using an arbitrary contact threshold, we used the average distance between centroids of adjacent steps as the cut-off distance for calling a contact/loop. We calculated this threshold based on all NT cells for the ~2.5 Mb sized domains on chr3 (th=256 nm) and chr6 (th=238 nm) that we imaged. For Ring1B and EED degron NT cells, th= 196 nm for plots in Figure S3.

t-SNE analyses DNA and RNA

t-SNE analyses in Figures 1 and S2 were done on the 3rd replicate of the data combining all imaged conditions (CTCF-AID NT, CTCF-AID +4h Aux, RAD21-AID NT, RAD21-AID +4h Aux and E14 NT). In these cells we also labeled Geminin by immunofluorescence, as described above, to distinguish G1 (defined as cells with the lowest 25% of Geminin) and G2 cells (with Geminin levels in the highest 35%). For t-SNE analyses in Figure S3C, we used all NT cells (CTCF-AID NT, RAD21-AID NT, E14 NT) merged across all replicates to match the hub analysis in Figure 3.

To avoid computational challenges from missing data in the t-SNE analysis, any missing points in each polymer path were first linearly interpolated from the x,y,z positions of the observed flanking positions. Any traces with less than 50% of the points detected above the required confidence threshold for calling a point were excluded from the analysis. The remaining traces were converted into single cell distance maps, which were then transformed into linear vectors. We performed t-SNE using the builtin Matlab^(TM) R2022b function t-SNE to project the resulting array N² of vectors into a two dimensional representation (where N=73 for the chr6 region studied and N=93 for the chr3 region studied). The cell type and cell-cycle state of each trace was denoted by color.

For the analysis of mRNA expression by t-SNE, in Figure 6, we created a vector for each cell recording the number of mRNA transcripts observed for each of the 12 genes assayed. We then used the builtin Matlab^(TM) R2022b function t-SNE to project these data into a 2-dimensional t-SNE representation.

Three-way contact analyses

For the three-way CTCF contact analyses in Figure 3, we picked the 3 CTCF sites for Hoxa (readouts 23, 46, 57, Tables S1 and S2) and Sox2 regions (readouts 45, 49, 61, Tables S1 and S2). We calculated the frequency of chromosomes with loops between sites 1-2 and 2-3. This frequency was normalized for detection efficiency for these pairs. We then shifted barcode positions 8 steps (with each step= 30 kb) in each direction and performed the same calculation for each shift. The expected frequencies were generated by multiplying the frequency for the pairs (frequency(1,2) * frequency (2-3)) and dividing by their detection efficiency.

We performed bootstrapping to estimate the confidence intervals for the contact frequencies. Bootstrapping was done by randomly sampling with replacement from the data. The height bars in the barplot (Figures 3B and S3H) correspond to the mean and the error bars correspond to the 25th and 75th quantiles. Thus, error bars that do not overlap reflect contact-frequencies that were distinct in 94% of resamplings (94 = 1 - 0.25²). We used 200 resampling draws in our bootstrapping, and noted more resamplings made little difference on the spread.

Identification of hub-containing chromosomes

We define as ‘hub traces’ all chromosomes with 3-way contacts for any 3 out of 5 CBSs (corresponding to readouts 15, 23, 37, 46, 57 for chr6; and readouts: 21, 45, 49, 61, 76 for chr3). For centrality analysis we calculated the centroid of each hub-trace and computed the distance (in nm) for each readout in the trace relative to the centroid. For Figure 3F, we plotted the median distance to centroid across all hub traces. We then computed the loop frequency for these CBS hub-containing chromosomes (Figures 3H and S3A) and loop difference between all CBS-hub and all NT traces (Figure S3B).

Entropy

For a given chromosome trace and each readout in the trace, we calculated the 3D distance (r) to all other readouts. Across all traces and for each pair of readouts (i,j), this became a distribution of distances $D_{i,j}$, which was then normalized by the number of traces (N) to obtain: $P_{i,j} = D_{i,j}/N$. The entropy (S) for the readout pair i,j was then computed by summing over all distances,

$r : S_{i,j} = - \sum_r (P_{i,j} \times \log_2(P_{i,j}))$. For each readout i , we then computed the average entropy: $S_i = \text{mean}(S_{i,j})$. For Figure 6B, we plotted the difference in S per barcode between NT cells and cells without CTCF or RAD21.

Compartment analysis using Pearson's Matrix

Compartmentalization was analyzed in the ORCA data starting from the median pairwise distance matrices, \mathbf{O} , for both the ~30 Mb scale and whole chromosome (~150 Mb) data. The “expected” distance was computed by averaging the 3D distance for all loci pairs which had the same genomic spacing. This produces a matrix, \mathbf{E} , with a smooth decay from the main diagonal. We then divided the observed distances by the expected distances to create a new matrix, \mathbf{N} , $N_{i,j} = O_{i,j}/E_{i,j}$. Finally, we computed the Pearson Matrix \mathbf{P} , such that $P_{i,j}$ is Pearson’s correlation coefficient between row i and column j of matrix \mathbf{N} . This parallels the original analysis of compartmentalization described for Hi-C, though using our distance measures in place of the contact-frequency per bin.²⁸

We note that the Hi-C and ORCA compartment analysis were computed with an important difference. The Hi-C compartment analysis at the 30 and 150 Mb scale uses reads from every part of the 30Mb (150 Mb) interval. In contrast, the ORCA data looks exclusively at particular 30 kb elements that skip through that domain at 1 Mb or 5 Mb intervals. Thus, substantial parts of the genome driving the correlation signal in the Hi-C data are not included. We note that our calculation using Hi-C data that focused only on the interactions between the 30 kb windows covered by the ORCA experiments were too sparsely populated to permit detection of compartments. Expanding these to 120 kb bins resulted in only minor improvement, and thus we elect to show the Hi-C compartmentalization computed using all the data. Thus, some qualitative differences in the position/distribution of the compartment boundaries likely reflects the contributions of genomic sequences not covered in our imaging experiments, though the sparsity of the Hi-C data makes this difficult to quantify precisely.

We used compartment calls in Bonev et al.⁷⁰ (Table S3) to map regions imaged by ORCA at the 150 Mb scale to A or B compartments.

Compartment clustering in single traces

A and B readouts were annotated according to compartment annotations (Table S3). DBSCAN was used to cluster between A or B readouts, using the built-in MatlabTM R2022b function dbscan, with a minimum cluster size of 2 and a threshold distance equal to the average consecutive-step distance of the trace.

Published genomic data

Hi-C data

We examined Hi-C experiments in mESCs from Nora et al.¹ for CTCF degradation, from Rhodes et al.⁴ for Rad21 degradation. This data was loaded in the processed Hi-C.cool files from either GEO (GSE98671) or ArrayExpress (E-MTAB-7816) respectively. We used Cooler⁷⁵ to export normalized tables directly using the cooler ‘dump’ command for the coordinates that match our probes. We then downsampled the data by averaging bins to match the resolution of the probes used for ORCA (30 kb for the ~2.5 Mb scale, 1 Mb for the ~30 Mb scale and 5 Mb for the ~150 Mb scale probes).

ChIP data

CTCF and Ring1b ChIP-seq data is from Bonev et al.⁷⁰ RAD21 ChIP-seq data is from Arruda et al.⁷¹ Processed bigwig files from GEO (GSE96107 for CTCF and Ring1b or GSM4280494 for RAD21) were viewed in the UCSC genome browser.

Supplemental information

**Loop stacking organizes genome folding
from TADs to chromosomes**

Antonina Hafner, Minhee Park, Scott E. Berger, Sedona E. Murphy, Elphège P. Nora, and Alistair N. Boettiger

Figure S1 related to Figure 1

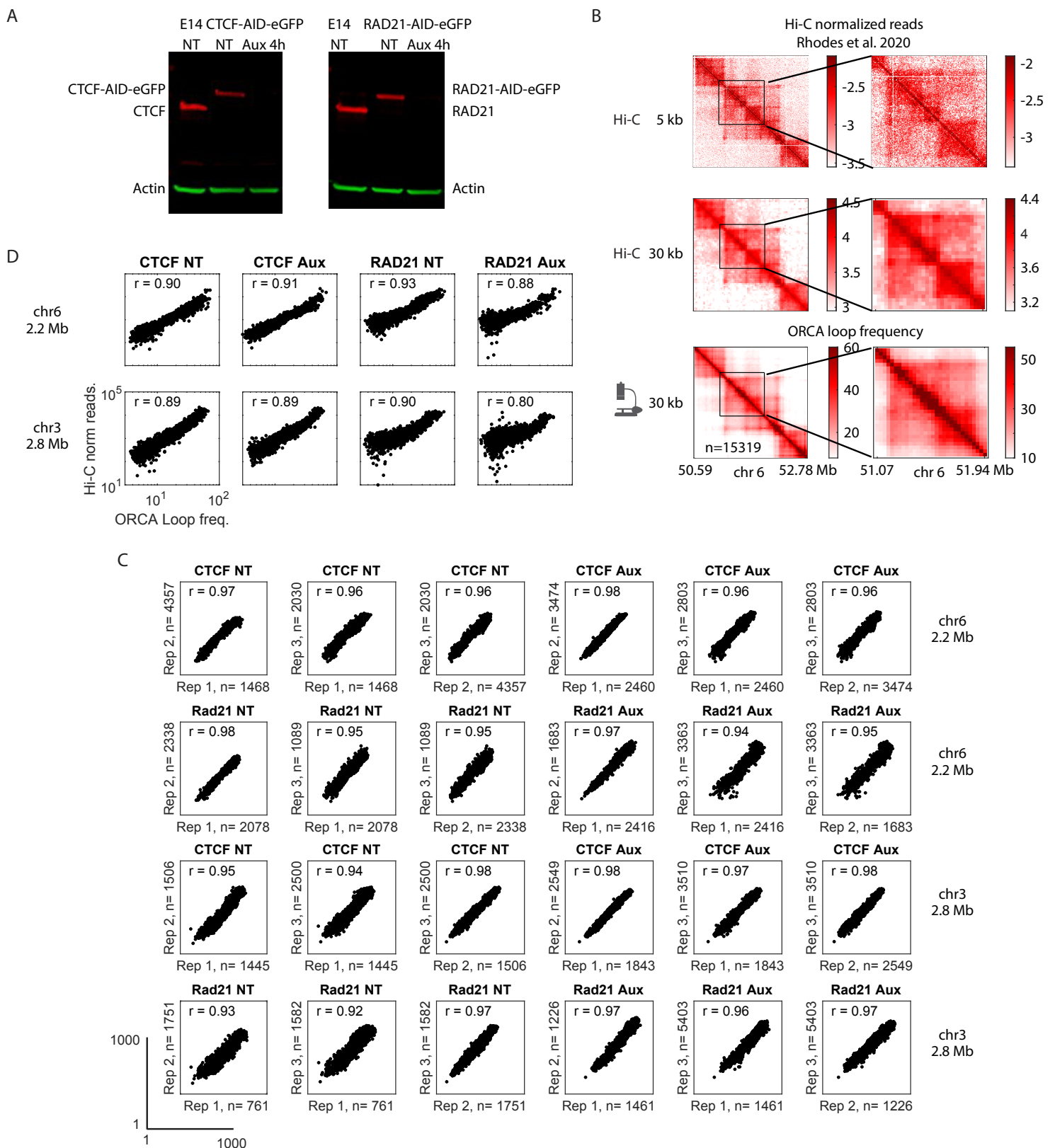


Figure S2 related to Figure 2

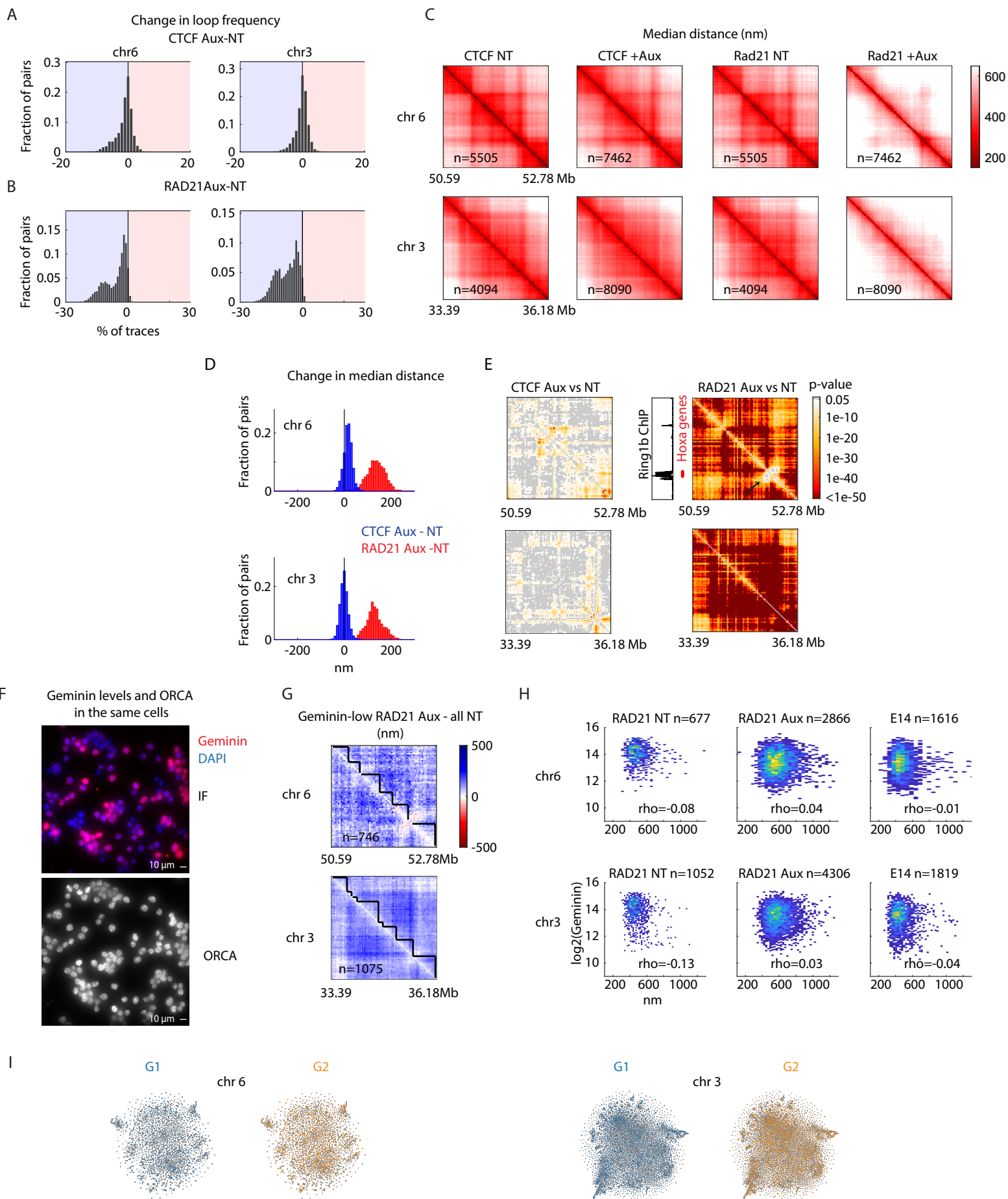


Figure S3 related to Figure 3

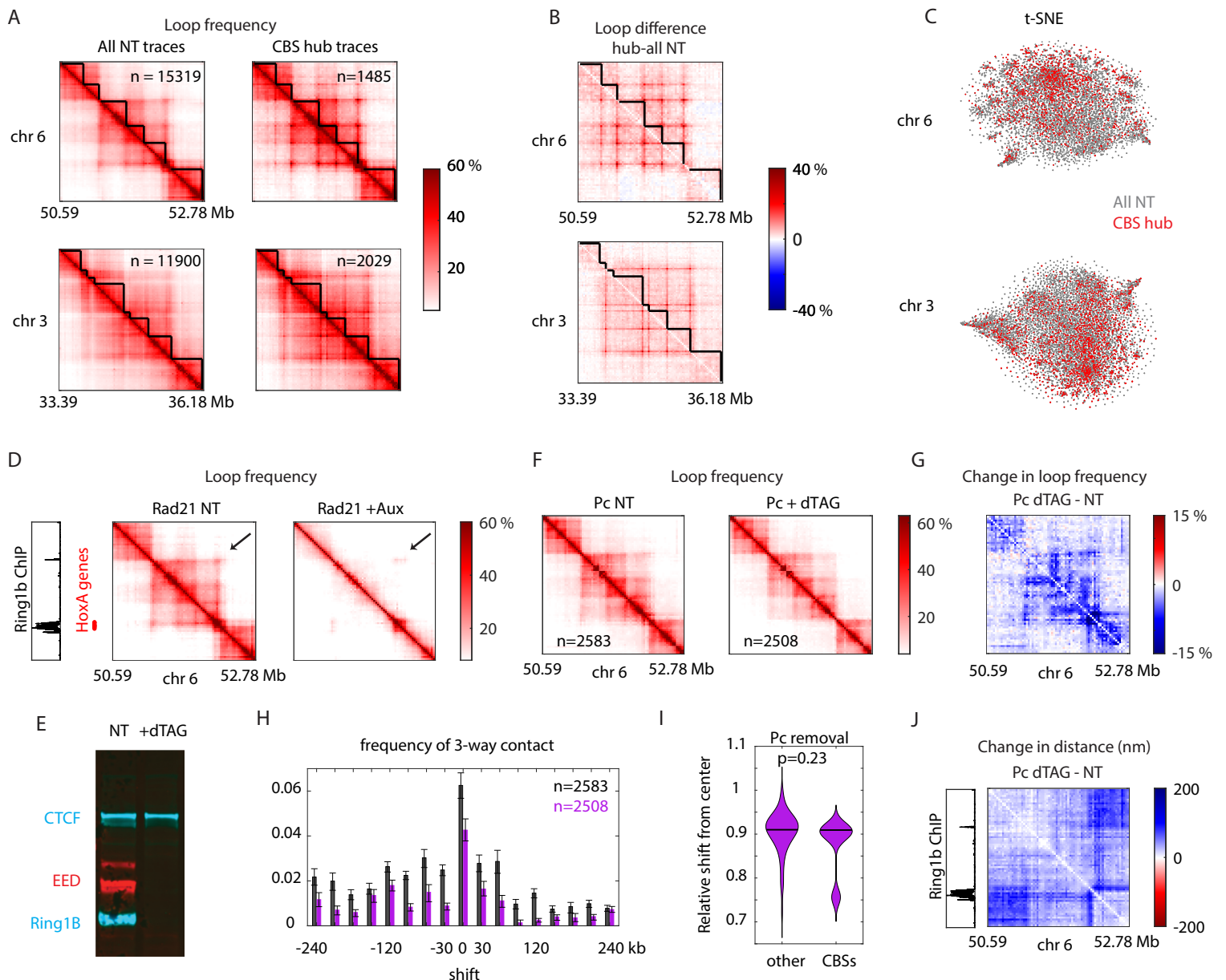
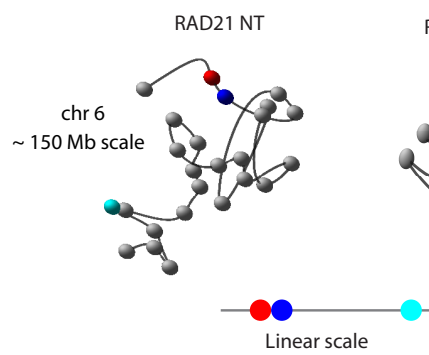
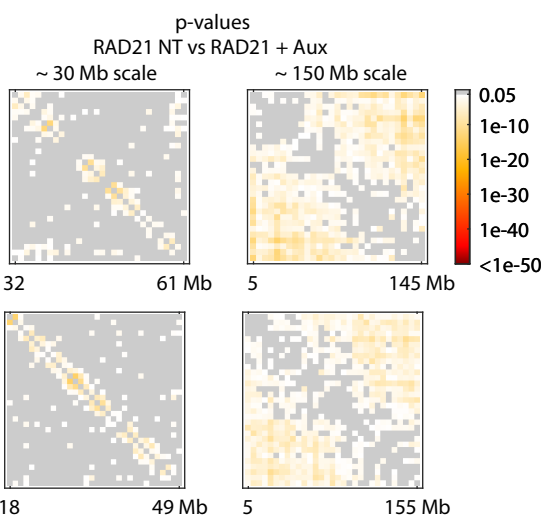


Figure S4 related to Figure 4

A



C



B

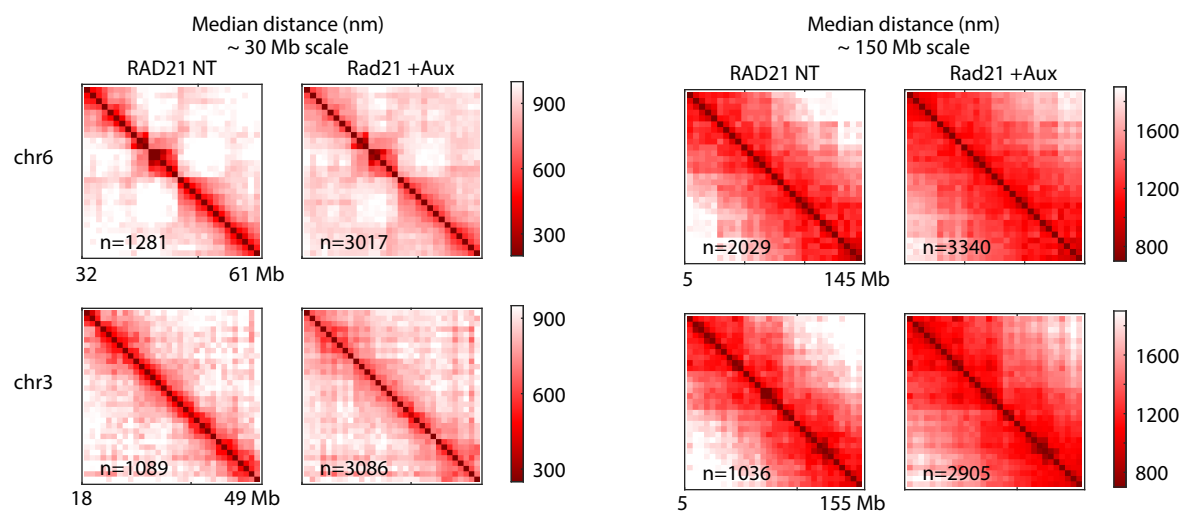


Figure S5 related to Figure 5

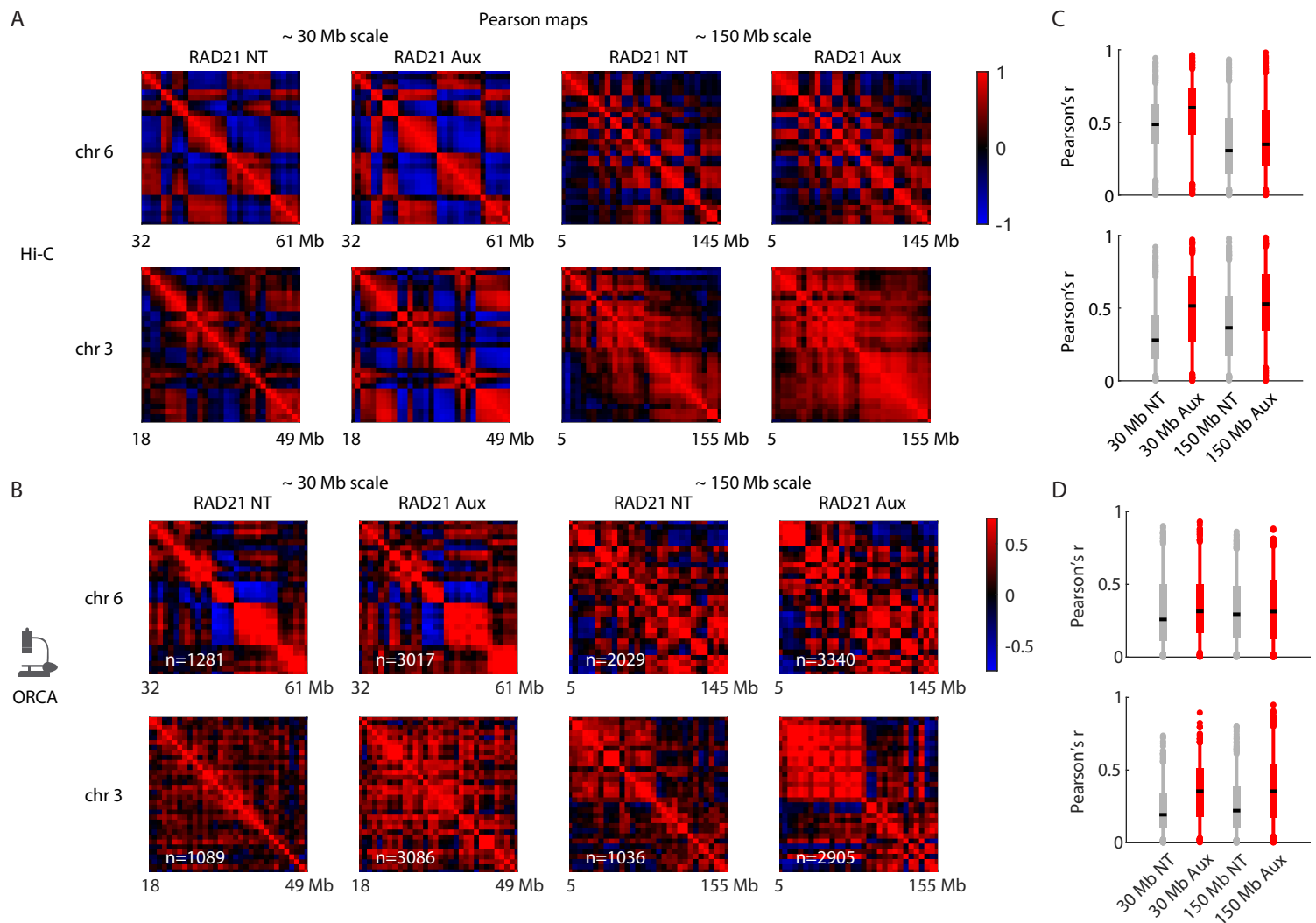


Figure S6 related to Figure 6

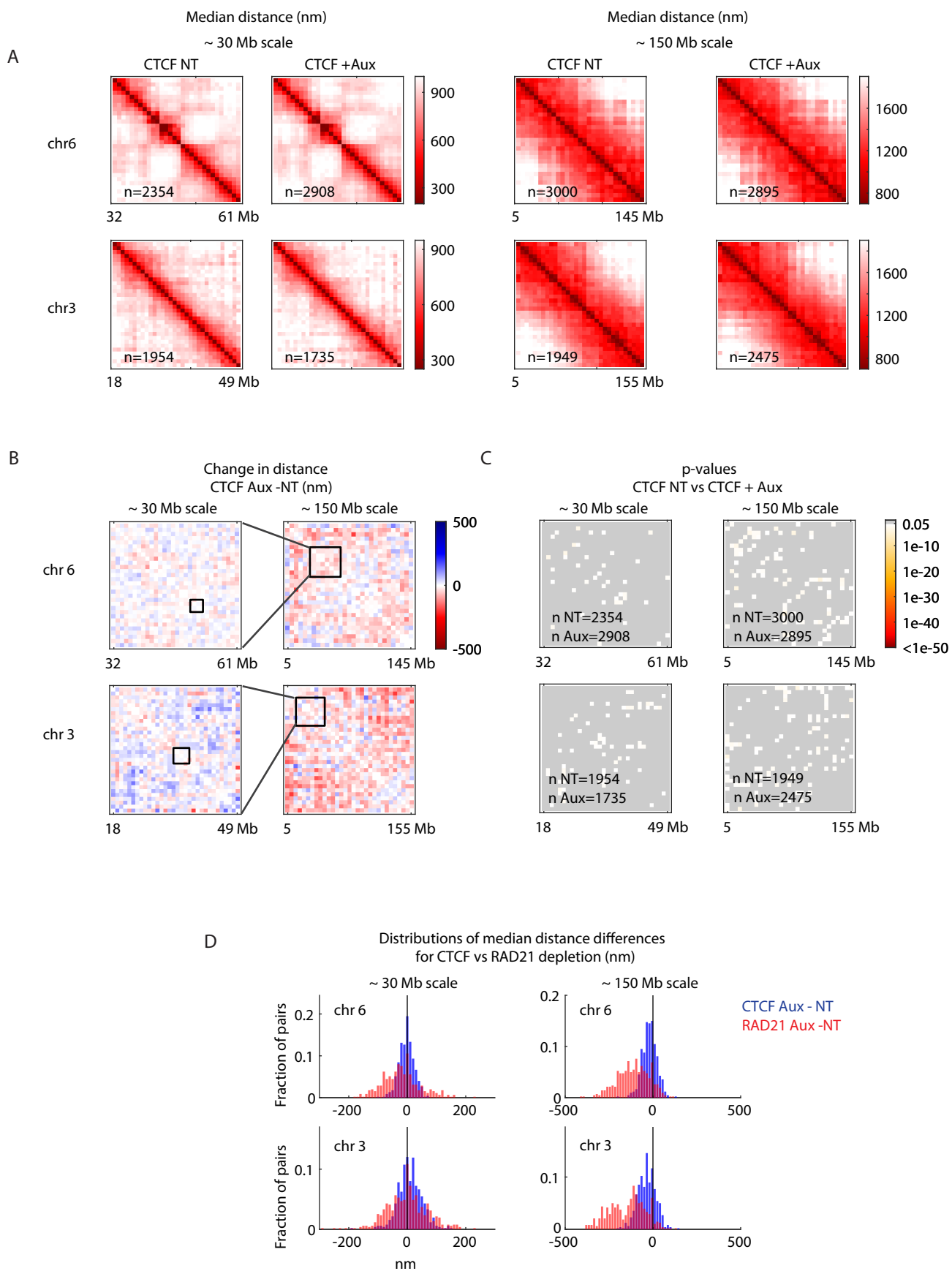


Figure S1 | Comparison across ORCA replicates and with Hi-C, Related to Figure 1. **A.** Western blot labeling Actin (loading control) and either CTCF or Cohesin in the parental E14 cell line and in the CTCF-AID-eGFP or RAD21-AID-eGFP cells, with or without auxin treatment. **B.** Hi-C data for chr 6, 2.2 Mb region and a ~900 kb region from 4 at either 5 kb or 30 kb resolution. The same regions are shown for the ORCA data. **C.** Scatter plots of inter-barcode distances, in nanometers, comparing reproducibility among three replicates labeling the chr6 or chr3 domains. Median distance is plotted for each barcode pair against the pairwise median distance in a different replicate. Pearson's correlation coefficient, r , is shown on the plot. The lower left plot shows the axis scale and the same scale was used for all plots. **D.** Scatter plots for ORCA loop frequencies vs Hi-C contact with Pearson's r is indicated on the plots.

Figure S2 | Quantification of effects of CTCF or cohesin depletion on genome folding, Related to Figure 2. **A-B.** Distribution of difference in loop frequency upon CTCF depletion (A) or cohesin depletion (B). **C.** Median distance maps for CTCF NT, CTCF +Aux, RAD21 NT and RAD21 +Aux conditions. **D.** Comparison of median distance differences between NT or +Aux conditions for either CTCF (blue) or RAD21 (red). **E.** P-values computed using Wilcoxon rank sum for each pairwise distance distribution between auxin treated and untreated cells. Arrows point to the Ring1B coated region on the heatmap that did not significantly change upon cohesin depletion and the corresponding Ring1B (member of the Polycomb complex) ChIP signal from 21 as well as the position of Hoxa genes. **F.** Example field of view of DAPI and immunofluorescent staining of Geminin and ORCA fiducial staining for the same cells. **G.** Difference in median distance between the Geminin-low population for the RAD21 auxin treated cells (number of cells on the plot) and all RAD21 untreated cells. **H.** Scatter plot of median distance (over all pairs) in each chromosome relative to Geminin levels in the same cell. Spearman's correlation coefficient is indicated for each condition. **I.** t-SNE plots (as in Figure 1) with colors corresponding to either Geminin-low (G1) cells or Geminin high (G2) cells.

Figure S3 | Quantification of effects of Polycomb depletion on looping, 3D distance and multi-way interactions, Related to Figure 3. **A.** Loop frequency for all NT traces vs Loop frequency of only hub-chromosomes. **B.** Loop difference between hub-chromosomes and All NT traces. **C.** t-SNE analysis of all NT cells with CBS-hub traces in red. **D.** Loop frequency for RAD21 NT and RAD21 +Aux conditions and the corresponding Ring1B (member of the polycomb complex), ChIP signal from 21 as well as the position of Hoxa genes. Arrow points to the loop-dot between two Pc domains that remains after cohesin depletion. **E.** Western blot showing depletion of Ring1B and EED following dTAG treatment (8h, 500nM) reproduced from ²⁵. **F.** Loop frequency from Pc NT or Pc depleted cells. **G.** Difference in loop frequency between Pc depleted and NT cells. **H.** Quantification of 3-way contacts in Pc NT (black) and in Pc +dTAG

cells (purple), as in Figure 3B. **I.** Fold change in central positioning upon Pc depletion for CBSs relative to other readouts. **J.** Difference in median distance between Pc dTAG and Pc NT cells.

Figure S4 | Cohesin depletion affects 3D structure at ~30 Mb and ~150 Mb scale, Related to Figure 4. **A.** Example of a trace at the 150 Mb scale from NT or RAD21 +Aux cells. Red and blue spheres mark positions of adjacent readouts (5 Mb apart), while the cyan sphere is 100 Mb away. Tube radius is 15 nm, sphere radius is 100 nm. **B.** Median distance maps for RAD21 NT and RAD21+Aux cells at ~30 Mb and ~150 Mb scales. **C.** P-values computed using Wilcoxon rank sum for each pair of barcodes between auxin-treated and untreated cells.

Figure S5 | ORCA, like Hi-C, shows compartment strengthening after depletion of cohesin, Related to Figure 5. **A.** Hi-C and **B.** ORCA Pearson maps for the ~30 Mb and ~150 Mb scales in RAD21 untreated or auxin treated cells. **C-D.** Distribution of Pearson correlation coefficients for Hi-C⁴ (C) and ORCA (D).

Figure S6 | CTCF depletion leads to less change in physical distance than cohesin depletion, Related to Figure 6. **A.** Median distance maps for ~30 Mb and ~150 Mb scales for CTCF NT or CTCF +Aux conditions. **B.** Median distance difference maps for CTCF Aux - CTCF NT cells at ~30 Mb and ~150 Mb scales. **C.** P-values computed using Wilcoxon rank sum for each pair between CTCF auxin-treated and untreated cells at different genomic scales. **D.** Distribution of median distance differences between auxin-treated and untreated cells for either CTCF (blue) or RAD21 (red).